Cell Metabolism

Article

Two independent respiratory chains adapt OXPHOS performance to glycolytic switch

Graphical abstract

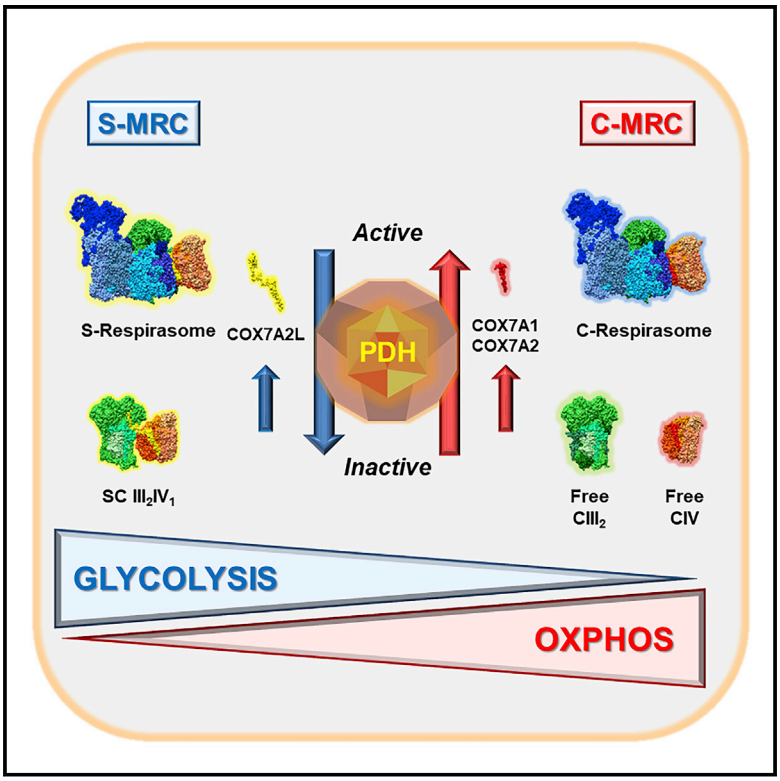

Highlights

- COX7A isoforms drive structurally distinct respiratory chains: C-MRC and S-MRC
- C-MRC and S-MRC display different bioenergetic properties
- C-MRC is favored when the PDH complex is activated, promoting OXPHOS
- Metabolic shift toward glycolysis stabilizes SCAFI and the S-MRC

Authors

Erika Fernández-Vizarra, Sandra López-Calcerrada, Ana Sierra-Magro, ..., Massimo Zeviani, Michael T. Ryan, Cristina Ugalde

Correspondence

erika.fernandezvizarra@unipd.it (E.F.-V.), cugalde@h12o.es (C.U.)

In brief

Fernández-Vizarra et al. show the co-existence of two separated mitochondrial respiratory chain (MRC) organizations in human cells driven by distinct COX7A isoforms. The prevalence of either organization is modulated by the activation state of the pyruvate dehydrogenase complex, which arises as a major metabolic regulator of MRC structure and function.

Fernández-Vizarra et al., 2022, Cell Metabolism *34*, 1–17
November 1, 2022
https://doi.org/10.1016/j.cmet.2022.09.005

CellPress

Please cite this article in press as: Fernández-Vizarra et al., Two independent respiratory chains adapt OXPHOS performance to glycolytic switch, Cell Metabolism (2022), https://doi.org/10.1016/j.cmet.2022.09.005

Cell Metabolism

CellPress

Article

Two independent respiratory chains adapt OXPHOS performance to glycolytic switch

Erika Fernández-Vizarra,[1,2,3,11,*] Sandra López-Calcerrada,[4] Ana Sierra-Magro,[4] Rafael Pérez-Pérez,[4] Luke E. Formosa,[5] Daniella H. Hock,[6] María Illescas,[4] Ana Peñas,[4] Michele Brischigliaro,[3] Shujing Ding,[1] Ian M. Fearnley,[1] Charalampos Tzoulis,[7] Robert D.S. Pitceathly,[8] Joaquín Arenas,[4,9] Miguel A. Martín,[4,9] David A. Stroud,[6,11] Massimo Zeviani,[1,2,10,11] Michael T. Ryan,[5,11] and Cristina Ugalde[4,9,11,12,*]

[1]Medical Research Council, Mitochondrial Biology Unit, University of Cambridge, Cambridge CB2 0XY, UK
[2]Veneto Institute of Molecular Medicine, 35129 Padova, Italy
[3]Department of Biomedical Sciences, University of Padova, 35131 Padova, Italy
[4]Instituto de Investigación Hospital 12 de Octubre, Madrid 28041, Spain
[5]Department of Biochemistry and Molecular Biology, Monash Biomedicine Discovery Institute, Monash University, 3800 Melbourne, Australia
[6]Department of Biochemistry and Pharmacology, Bio21 Molecular Science and Biotechnology Institute, University of Melbourne, 3052 Melbourne, Australia
[7]Neuro-SysMed Center of Excellence for Clinical Research in Neurological Diseases, Department of Neurology, Haukeland University Hospital and Department of Clinical Medicine, University of Bergen, Pb 7804, 5020 Bergen, Norway
[8]Department of Neuromuscular Diseases, UCL Queen Square Institute of Neurology and The National Hospital for Neurology and Neurosurgery, London WC1N 3BG, UK
[9]Centro de Investigación Biomédica en Red de Enfermedades Raras (CIBERER), U723 Madrid, Spain
[10]Department of Neurosciences, University of Padova, 35128 Padova, Italy
[11]Senior author
[12]Lead contact
*Correspondence: erika.fernandezvizarra@unipd.it (E.F.-V.), cugalde@h12o.es (C.U.)
https://doi.org/10.1016/j.cmet.2022.09.005

SUMMARY

The structural and functional organization of the mitochondrial respiratory chain (MRC) remains intensely debated. Here, we show the co-existence of two separate MRC organizations in human cells and postmitotic tissues, C-MRC and S-MRC, defined by the preferential expression of three COX7A subunit isoforms, COX7A1/2 and SCAFI (COX7A2L). COX7A isoforms promote the functional reorganization of distinct co-existing MRC structures to prevent metabolic exhaustion and MRC deficiency. Notably, prevalence of each MRC organization is reversibly regulated by the activation state of the pyruvate dehydrogenase complex (PDC). Under oxidative conditions, the C-MRC is bioenergetically more efficient, whereas the S-MRC preferentially maintains oxidative phosphorylation (OXPHOS) upon metabolic rewiring toward glycolysis. We show a link between the metabolic signatures converging at the PDC and the structural and functional organization of the MRC, challenging the widespread notion of the MRC as a single functional unit and concluding that its structural heterogeneity warrants optimal adaptation to metabolic function.

INTRODUCTION

The oxidative phosphorylation (OXPHOS) system provides most of the chemical energy (ATP) used by cells and tissues through the concerted action of five multiprotein enzyme complexes embedded in the lipid bilayer of the inner mitochondrial membrane. The first four enzyme complexes (CI–CIV) form the mitochondrial respiratory chain (MRC), which acts in concert with two mobile electron carriers, coenzyme Q (CoQ) and cytochrome *c* (cyt *c*), to facilitate electron transfer from reducing equivalents to molecular oxygen. This process powers generation of a proton gradient across the inner mitochondrial membrane that is used by the ATP synthase (complex V) to drive ATP synthesis. It is widely accepted that MRC complexes I, III_2, and IV (CI, $CIII_2$, and CIV) can associate in different combinations to form supramolecular assemblies known as supercomplexes (SCs) that co-exist with unbound $CIII_2$ and CIV (Cruciat et al., 2000; Schägger and Pfeiffer, 2000). Complexes I, III_2, and IV preferentially associate in structures known as respirasomes (or SC I+III_2+IV), whose functional relevance remains a matter of active debate (Cogliati et al., 2021; Hirst, 2018; Javadov et al., 2021; Letts and Sazanov, 2017; Lobo-Jarne and Ugalde, 2018; Milenkovic et al., 2017; Vercellino and Sazanov, 2022). SCs have been proposed to confer functional advantages to the MRC by increasing its overall catalytic activity and by reducing electron leakage, leading to reactive oxygen species (ROS) formation. This would be achieved through a highly controlled electron transfer through the MRC complexes and

Please cite this article in press as: Fernández-Vizarra et al., Two independent respiratory chains adapt OXPHOS performance to glycolytic switch, Cell Metabolism (2022), https://doi.org/10.1016/j.cmet.2022.09.005

by the segregation of two distinct CoQ pools (Bianchi et al., 2004; Lapuente-Brun et al., 2013; Lenaz and Genova, 2007, 2009; Lopez-Fabuel et al., 2016). In fact, the physical association of $CIII_2$ with CIV in SCs has been shown to accelerate electron-transfer kinetics via cyt *c* (Berndtsson et al., 2020; Stuchebrukhov et al., 2020; Vercellino and Sazanov, 2021). However, structural and biophysical data obtained for the respirasome, as well as for SC I+III_2 and SC III_2+IV, refuted the possibilities of both "substrate channeling" (Hirst, 2018; Letts et al., 2019; Vercellino and Sazanov, 2021) and partitioning of the CoQ or cyt *c* pools (Blaza et al., 2014; Fedor and Hirst, 2018; Trouillard et al., 2011). Alternative ideas propose that, regardless of its catalytic properties, respirasome formation may protect mitochondrial function either by stabilizing the individual complexes (Lobo-Jarne and Ugalde, 2018) or by preventing protein aggregation of the densely packed inner mitochondrial membrane (Hirst, 2018; Milenkovic et al., 2017). Therefore, at present, how SCs in general—and respirasomes in particular—may constitute a functionally advantageous organization of the mammalian MRC is unknown.

In addition, the regulatory mechanisms of SC biogenesis, by which the structural reorganization of the MRC can adapt OXPHOS function to different energy requirements, remain unclear (Fernández-Vizarra and Ugalde, 2022). The prevalent ("plasticity") model proposes the structural organization of the MRC as the dynamic association of fully preassembled individual MRC complexes I, III_2, and IV into SCs to modulate MRC function according to physiological energy demands (Acín-Pérez et al., 2008). However, growing evidence supports a "cooperative-assembly model," in which SC biogenesis is achieved through a number of regulatory checkpoints at intermediate steps in the assembly of individual complexes I, III, and IV (Fang et al., 2021; Fernández-Vizarra and Ugalde, 2022; Lobo-Jarne et al., 2020; Protasoni et al., 2020; Timon-Gomez et al., 2020; Vercellino and Sazanov, 2021). Both the plasticity and cooperative-assembly models are compatible with the known structures of mammalian SCs, in which the COX7A protein-family members bridge the physical association of CIV with complexes I and III_2 (Gu et al., 2016; Guo et al., 2017; Letts et al., 2016; Sousa et al., 2016; Wu et al., 2016). This protein family includes COX7A1 and COX7A2, the tissue-specific isoforms of the CIV structural COX7A subunit, expressed in heart/muscle and in liver/ubiquitously, respectively (Sinkler et al., 2017). A third isoform, COX7A2L, which we render here as "SC-associated factor 1" (SCAFI), was thought to be essential for CIV binding in both SC III_2+IV and respirasomes (Ikeda et al., 2013; Lapuente-Brun et al., 2013). The recent resolution of the mammalian SC III_2+IV structure (Vercellino and Sazanov, 2021) confirmed the structural role of SCAFI in the biogenesis of this low-abundance SC (Cogliati et al., 2016; Mourier et al., 2014; Perez-Perez et al., 2016). However, the functional relevance of SCAFI in respirasome biogenesis remains questioned because the predominant respirasome population contains COX7A1/2 (Fernandez-Vizarra et al., 2021; Vercellino and Sazanov, 2021; Zong et al., 2018). Interestingly, SCAFI loss does not drastically affect the overall bioenergetic capacity of the mammalian MRC (Lobo-Jarne et al., 2018; Mourier et al., 2014), although it seems to be involved in some metabolic alterations associated with a marginal MRC dysfunction (Calvo et al., 2020; Garcia-Poyatos et al., 2020; Shiba et al., 2017). These observations suggest the co-existence of different regulatory pathways for MRC biogenesis and function, possibly driven by the dynamic interchange of COX7A isoforms within the MRC structures in yet undefined ways (Cogliati et al., 2016; Letts and Sazanov, 2017).

In this work, we dissect the mechanisms regulating the structural and functional organization of the human MRC by modulating the expression of the COX7A subunit isoforms. We demonstrate the co-existence of two structurally and functionally independent organizations of the MRC complexes and SCs in human cell lines and postmitotic tissues, each entirely depending on the prevalent COX7A subunit isoform. Importantly, these structurally distinct MRC organizations display different functional properties involved in the adaptive response of OXPHOS efficiency to the metabolic switch between oxidative and anaerobic (glycolytic) metabolisms. Specifically, our data reveal that the COX7A-isoform-dependent structural organization of the MRC is tightly regulated by the activity of the pyruvate dehydrogenase complex (PDC), which modulates the structural redundancy of the MRC to optimize OXPHOS performance under varying metabolic settings.

RESULTS AND DISCUSSION

SCAFI stabilization depends on COX7A2 levels

We used CRISPR-Cas9 genome editing to disrupt the genes encoding COX7A2 and SCAFI (Figure S1A), the two COX7A subunit isoforms expressed in HEK293T cells (Fernandez-Vizarra et al., 2021; Lobo-Jarne et al., 2018, 2020; Zong et al., 2018). As previously shown (Fernandez-Vizarra et al., 2021), the steady-state levels of COX7A2 were normal in $SCAFI^{KO}$ cells. In contrast, SCAFI protein levels were markedly increased in $COX7A2^{KO}$ cells (Figure 1A) relative to the control and to another cell line lacking CIV (CIV^{KO}) (Figure S1A). This increase in protein levels happened without a parallel upregulation of *SCAFI* transcripts (Figure 1B). We investigated this mechanism further by treating wild-type (WT) and $COX7A2^{KO}$ cells for up to 24 h with the cytosolic protein translation inhibitor cycloheximide (CHX). Western blotting of mitochondrial lysates (Figure 1C) showed a steady decline of SCAFI levels in WT cells, but unaltered high levels of this protein in $COX7A2^{KO}$ cells, indicating that SCAFI is largely stabilized upon COX7A2 loss. Accordingly, stable isotope labeling by amino acids in cell culture (SILAC) and complexome profiling (CP)-based quantifications, in which the relative abundance of SCAFI was calculated based on the area under the curve (AUC) defined by the peptide intensity along the electrophoresis lane (Páleníková et al., 2021b), confirmed an overall 16-fold increase in SCAFI levels in $COX7A2^{KO}$ cells compared with the WT (Figure 1D, upper panels). The SCAFI peptide signals mainly colocalized with SC III_2+IV and with the SCAFI-containing respirasomes (Figures 1D [upper panels], 1E, and 2). Importantly, overexpression of $COX7A2^{FLAG}$ reverted the high SCAFI levels to nearly normal in the $COX7A2^{KO}$ cells and decreased SCAFI levels in WT cells (Figure S1B). Therefore, the degree of stabilization of SCAFI relies on COX7A2 protein levels. We then performed experiments on a double knockout (D^{KO}) cell line in which *COX7A2* harbored an indel, frameshift mutation, whereas the mutation in *SCAFI* (Figure S1A) predicted an in-frame deletion of eight amino acids (positions G25 to T32,

Please cite this article in press as: Fernández-Vizarra et al., Two independent respiratory chains adapt OXPHOS performance to glycolytic switch, Cell Metabolism (2022), https://doi.org/10.1016/j.cmet.2022.09.005

CellPress

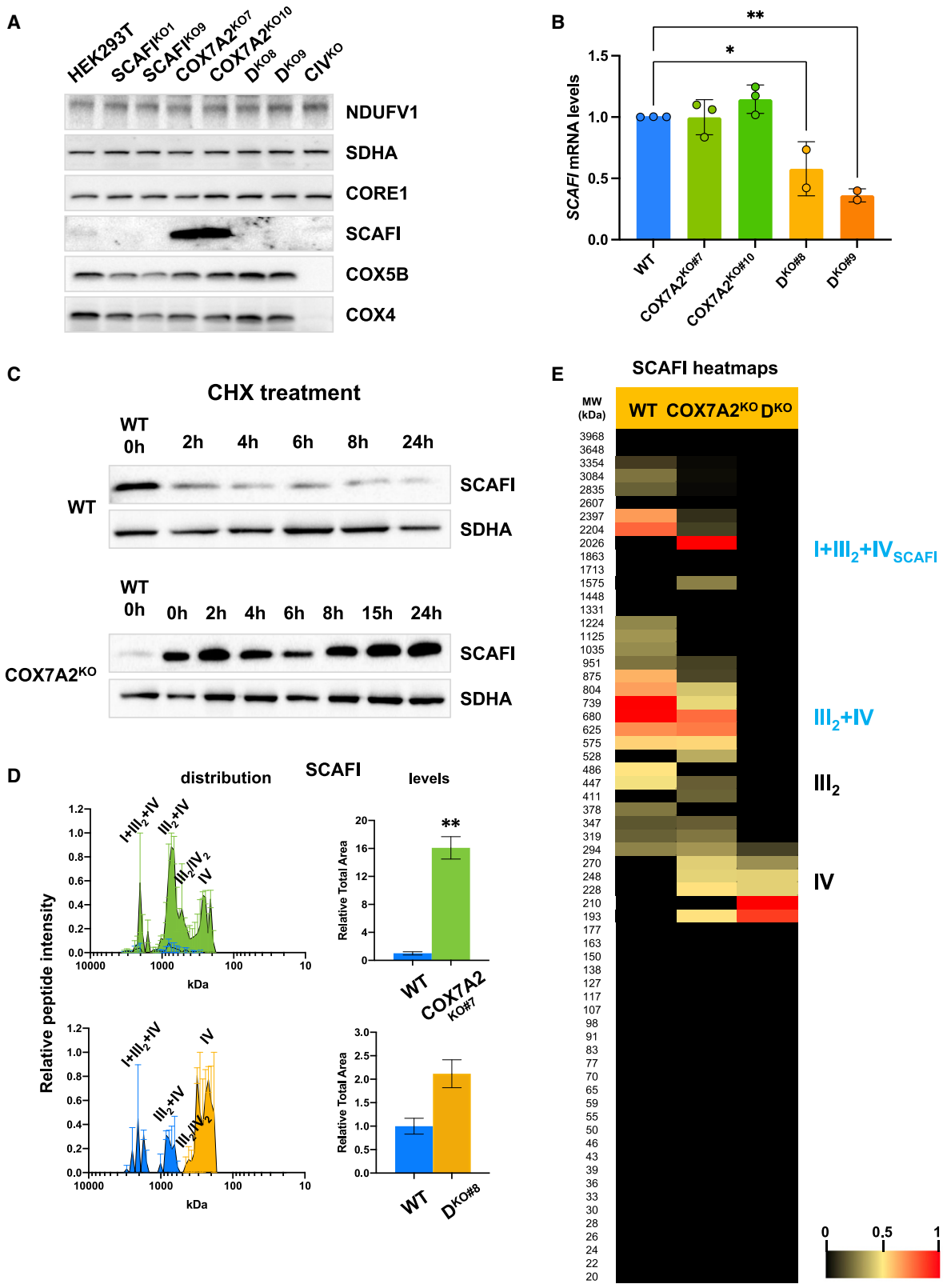

(legend on next page)

Please cite this article in press as: Fernández-Vizarra et al., Two independent respiratory chains adapt OXPHOS performance to glycolytic switch, Cell Metabolism (2022), https://doi.org/10.1016/j.cmet.2022.09.005

shown in red in Figure S1C), localized to its $CIII_2$-binding domain (Vercellino and Sazanov, 2021). This change reduced the stability of the protein, which was barely detectable by immunoblotting (Figures 1A and S1B), and also impaired its function, since it was unable to bind $CIII_2$ and form the SC III_2+IV (Figures 1D and 1E). Interestingly, the residual truncated SCAFI peptides co-localized exclusively with CIV subassemblies (Figures 1D and 1E). All detected SCAFI peptides in D^{KO} samples (in yellow in Figure S1C, respectively) spanned the CIV-binding C-terminal domain (Vercellino and Sazanov, 2021), whereas in WT cells, the detected peptides belonged to both the N- and C-terminal domains (in yellow and blue in Figure S1C). Despite a prominent decrease in *SCAFI* mRNA levels in D^{KO} cells (Figure 1B), truncated SCAFI levels were still 2-fold higher that in the WT (Figure 1D), a likely consequence of its stabilization promoted by COX7A2 downregulation. These data experimentally confirm the function of different domains of SCAFI protein; for instance, the CIV-binding role of the C terminus and the requirement of SCAFI to bind $CIII_2$ to promote the formation of SC III_2+IV (Vercellino and Sazanov, 2021).

Co-existence of two human respiratory chain organizations: C-MRC and S-MRC

Next, we used comprehensive SILAC-CP analyses (Páleníková et al., 2021a, 2021b) to investigate the consequences of SCAFI and COX7A2 ablation on the structural organization of the MRC (Figure 2). In all cell lines, active holo-CI was exclusively present in SC I+III_2 and respirasomes, whose electrophoretic mobility changed mainly because of the variable localization of $CIII_2$ and CIV in the context of the SC/respirasome structures (Figures 2, 3, and S2A–S2C). As previously reported (Fernandez-Vizarra et al., 2021; Lobo-Jarne et al., 2018), the $SCAFI^{KO}$ clones presented increased levels of free $CIII_2$ and SILAC-CP-based quantifications estimated a 30%–40% decrease in respirasome levels, with a major respirasome structure of ~1,500 kDa that exclusively contained COX7A2. We call this species SC I+III_2+IV_{COX7A2} or C-respirasome (in which C stands for COX7A2). These cells lacked SC III_2+IV (of ~700 kDa), presented normal abundance of free CIV, and accordingly, showed CIV activity only in free holo-CIV and in the C-respirasome (Figure S2A). In contrast, the $COX7A2^{KO}$ cells showed a complementary pattern, where the majority of redistributed $CIII_2$ and CIV associated with SCAFI. This pattern included two main structures, a very abundant SC III_2+IV which, according to SILAC-CP-based quantifications, contains ~8× more $CIII_2$ and 4× more CIV than the WT, and a large SCAFI-containing respirasome of ~1,800–2,000 kDa named SC I+III_2+IV_{SCAFI} or S-respirasome (in which S stands for SCAFI). Both structures displayed CIV activity (Figure S2A). The preferential interaction of SCAFI with SC III_2+IV was also demonstrated in mitochondria solubilized with the harsher detergent n-dodecyl-ß-D-maltoside (DDM), which disrupts the respirasome but maintains SC III_2+IV (Figure S3D). Finally, the D^{KO} clones presented active CI only in SC I+III_2, a structure of ~1,225 kDa, and accumulated a substantial amount of free $CIII_2$ (Figures 2, S2A, and S2C); D^{KO} cells also showed decreased amounts (Figure 2) and activity (Figure S2A) of CIV, which appeared to co-migrate with CIV subcomplexes that were also present, albeit at lower levels, in the $COX7A2^{KO}$ cells (Figures 2 and S2A).

These data suggest defective assembly of free CIV in the cells lacking COX7A2 (both $COX7A2^{KO}$ and D^{KO}). This was corroborated by SILAC-based quantitative mass spectrometry (Q-MS) of mitochondrial lysates (Figure 3A). While $SCAFI^{KO}$ samples (Fernandez-Vizarra et al., 2021) revealed normal CIV assembly (Figures 2 and 3A–3E, left panels), $COX7A2^{KO}$ mitochondria showed reduced levels of the CIV subunits that, together with COX7A2, form the MT-CO3 module (involved in the last steps of CIV assembly alongside NDUFA4) (Figures 3A, 3D, and 3E, center panels) (Hock et al., 2020; Timon-Gomez et al., 2020; Vidoni et al., 2017). The D^{KO} samples showed an even more prominent CIV defect (Figures 3A, 3D, and 3E, right panels), consistent with a severe reduction in the levels of CIV subunits involved in both the intermediate (MT-CO2 module) and last steps (MT-CO3 module and NDUFA4) of CIV assembly. In addition, in both $COX7A2^{KO}$ and D^{KO} cells there was a concomitant increase in the abundance of the CIV assembly factors COX15, CMC2, COA1, COX17, and PET117. This result clearly indicates the stalling of the CIV assembly process in both $COX7A2^{KO}$ and D^{KO} cell lines, which accumulate a labile CIV intermediate sensitive to DDM-detergent treatment (Figure S3D), most likely due to the loss of the stabilizing MT-CO3 module (Ogunjimi et al., 2000). Remarkably, the main structural difference between these two cell lines was the presence of fully assembled CIV (containing the MT-CO3 module and NDUFA4) almost exclusively

Figure 1. Loss of COX7A2 leads to SCAFI stabilization

(A) Immunodetection of SCAFI and of the MRC structural subunits NDUFV1 (CI), SDHA (CII), CORE1 (CIII), and COX4 and COX5B (CIV) on western blots of whole-cell lysates separated by SDS-PAGE.

(B) *SCAFI* mRNA levels, quantified by real-time PCR and normalized by *HPRT1* mRNA levels. Values represent mean ± SD from either 2 to 3 independent analyses per cell line, each with three experimental replicates. Individual data points are shown with overlaying dot plots. *$p < 0.05$ and **$p < 0.01$, one-way ANOVA and Dunnett's multiple comparisons tests.

(C) Immunodetection of SCAFI and SDHA on western blot SDS-PAGE analyses of mitochondrial extracts from cells treated for the indicated time points (in hours) with the cytosolic protein synthesis inhibitor cycloheximide (CHX).

(D) SILAC-CP profiles of SCAFI peptide distribution and abundance in WT (blue traces) versus either $COX7A2^{KO}$ cells (green traces) or D^{KO} cells (yellow traces). The relative SCAFI protein abundance was estimated by calculating the areas under the curve (AUCs) defined by the SCAFI peptide intensity peaks along the electrophoresis lanes in two SILAC-CP replicates. The x axis values show the apparent molecular weights along 64 blue native (BN) gel slices, and the y axis values show the relative peptide intensity. The relative total area graphs represent the sum of the AUCs defined by all the SCAFI peaks normalized to the control values (set to 1.0); **$p < 0.01$, unpaired Student's t test.

(E) SILAC-CP heatmaps showing the distribution and relative abundance of SCAFI peptides in SC I+III_2+IV_{SCAFI}, SC III_2+IV, dimeric CIII ($CIII_2$), and free CIV (IV). The peptide abundances for each protein were normalized to the highest intensity in the lane (set to 1). The color scale of normalized peptide intensities is indicated: 1 is red, the midpoint 0.5 is yellow, and 0 is black. The relative position of SCAFI peptides with regard to the migration patterns of MRC complexes I, III, and IV is detailed in Figure 2.

Please cite this article in press as: Fernández-Vizarra et al., Two independent respiratory chains adapt OXPHOS performance to glycolytic switch, Cell Metabolism (2022), https://doi.org/10.1016/j.cmet.2022.09.005

CellPress

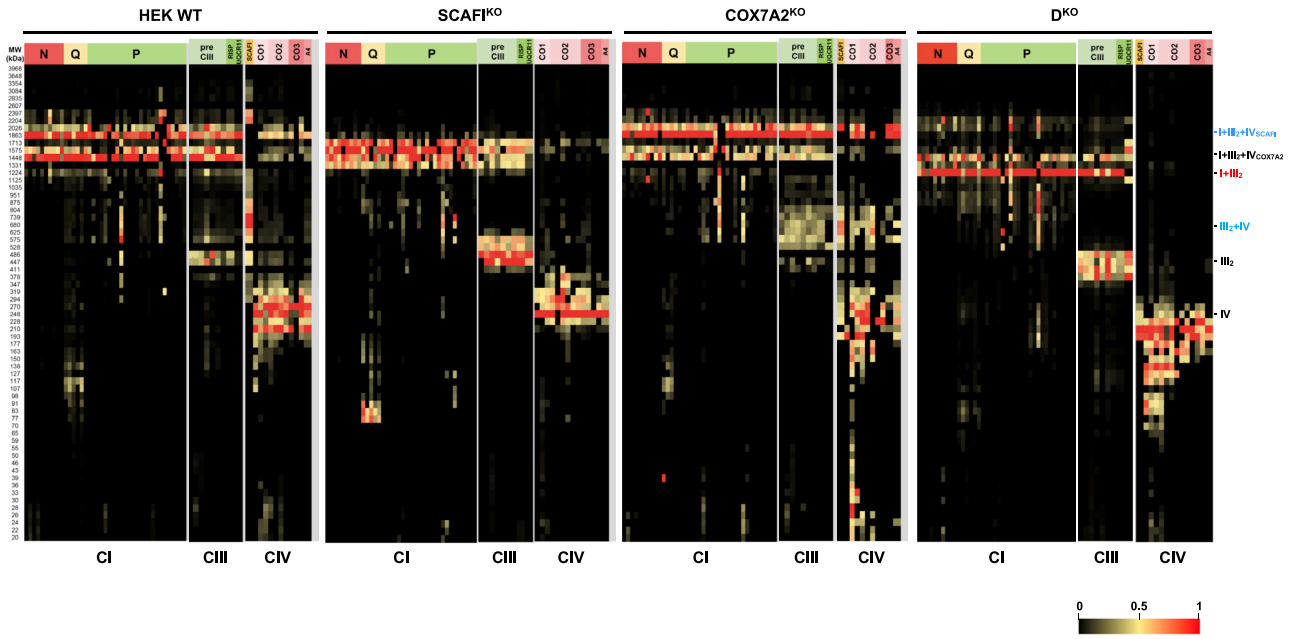

Figure 2. Protein profiles of the C-MRC and S-MRC organizations

SILAC-CP heatmaps showing the distribution and relative abundance of SCAFI (indicated with an orange label) and of MRC subunits from CI, $CIII_2$, and CIV. The peptide abundances for each protein were normalized to the highest intensity in the lane (set to 1). The color scale of normalized peptide intensities is indicated: 1 is red, the midpoint 0.5 is yellow, and 0 is black. N, subunits belonging to the CI NADH dehydrogenase module; Q, subunits belonging to the CI CoQ-binding module; P, subunits belonging to the CI proton translocation module; Pre-CIII, subunits assembling in the early and middle stages before the incorporation of the Rieske Fe-S protein (RISP) and UQCR11; CO1, CIV subunits belonging to the initial and MT-CO1 modules; CO2, the MT-CO2 module; CO3, the MT-CO3 module; A4, peripherally associated NDUFA4 subunit. Visible supercomplexes were indicated as follows: C-respirasomes, black text; S-respirasomes, blue text; SC I+III_2, red text; SC III_2+IV, blue text.

associated to SCs in the COX7A2^{KO} cells (Figures 2, 3B–3E, and S3A–S3C). In contrast, mutant SCAFI in the D^{KO} cells could not promote SCs formation, as it was unable to bind $CIII_2$ and to let the MT-CO3 module be incorporated into CIV.

Next, we followed the assembly kinetics of respiratory complexes and SCs after reversible inhibition of mitochondrial translation with doxycycline (Figure S4A). As expected, the COX7A2^{KO} cells showed preferential assembly of holo-CIV within SC III_2+IV, whereas SCAFI^{KO} cells efficiently incorporated CIV into the C-respirasome (Figure S4B). Notably, the biogenesis of the S-respirasome was significantly delayed relative to that of the C-respirasome. The sequential increase in SC III_2+IV levels, followed by holo-CIV and then by the S-respirasome, correlated with the progressive accumulation of SCAFI within these structures (Figure S4C). The nature of the apparent molecular mass shift of the S-respirasome remains enigmatic, as no obvious protein specifically co-migrating with this structure was identified in our CP-SILAC analyses, and the stoichiometry of CIV subunits in both types of respirasomes was the same (Figures 2, 3A–3E, and S3A–S3C). Overall, these data demonstrate that the COX7A isoforms play a dual role in CIV biogenesis, by promoting its maturation via incorporation of the MT-CO3 module and its stabilization into different SC structures.

In summary, COX7A2 and SCAFI promote two mutually exclusive structural organizations of the MRC (hereafter C-MRC and S-MRC, respectively) (Figure S5). The C-MRC, the only organization present in SCAFI^{KO} cells, is characterized by the biogenesis of the C-respirasome (SC I+III_2+IV_{COX7A2}), and of $CIII_2$ and CIV in free state. The S-MRC, promoted by SCAFI stabilization and prominent in COX7A2^{KO} cells, is characterized by the segregation of approximately half of $CIII_2$ and CIV within the S-respirasome (SC I+III_2+IV_{SCAFI}), the remaining half within SC III_2+IV, and residual amounts of free complexes. In normal conditions (i.e., WT cells) the C-MRC and S-MRC organizations co-exist, and both types of respirasomes are present in a proportion of ~70% C-respirasome versus ~30% S-respirasome (Fernandez-Vizarra et al., 2021). Importantly, the C-MRC and S-MRC organizations also co-exist in human differentiated tissues from control individuals, namely brain frontal cortex and skeletal muscle (Figures 4A and 4B). Quantifications of the relative amounts of complexes I, III_2, and IV in each of the CP peptide intensity peaks corresponding to the different assembly species (i.e., the SCs and individual complexes) revealed that the structural organization of the MRC is conserved between human brain (Figures 4A and 4C) and cultured cells (Figures 4E and 4F). This likely happens because COX7A2, and SCAFI to a lesser extent, are predominantly expressed in this specific tissue and cell types (Figure S5A), allowing two distinguishable MRC organizations to co-exist, one driven by COX7A2 and the other one by SCAFI. The situation changes in skeletal muscle, where COX7A1 transcript levels are one order of magnitude higher than those of COX7A2 and SCAFI (Figure S5A). In fact, no peptide corresponding to SCAFI was detected by MS in the CP analysis of skeletal muscle. Accordingly, this tissue shows an exclusive C-MRC organization driven by the prevalent COX7A1 isoform, which precludes the formation of the S-respirasome and SC

Please cite this article in press as: Fernández-Vizarra et al., Two independent respiratory chains adapt OXPHOS performance to glycolytic switch, Cell Metabolism (2022), https://doi.org/10.1016/j.cmet.2022.09.005

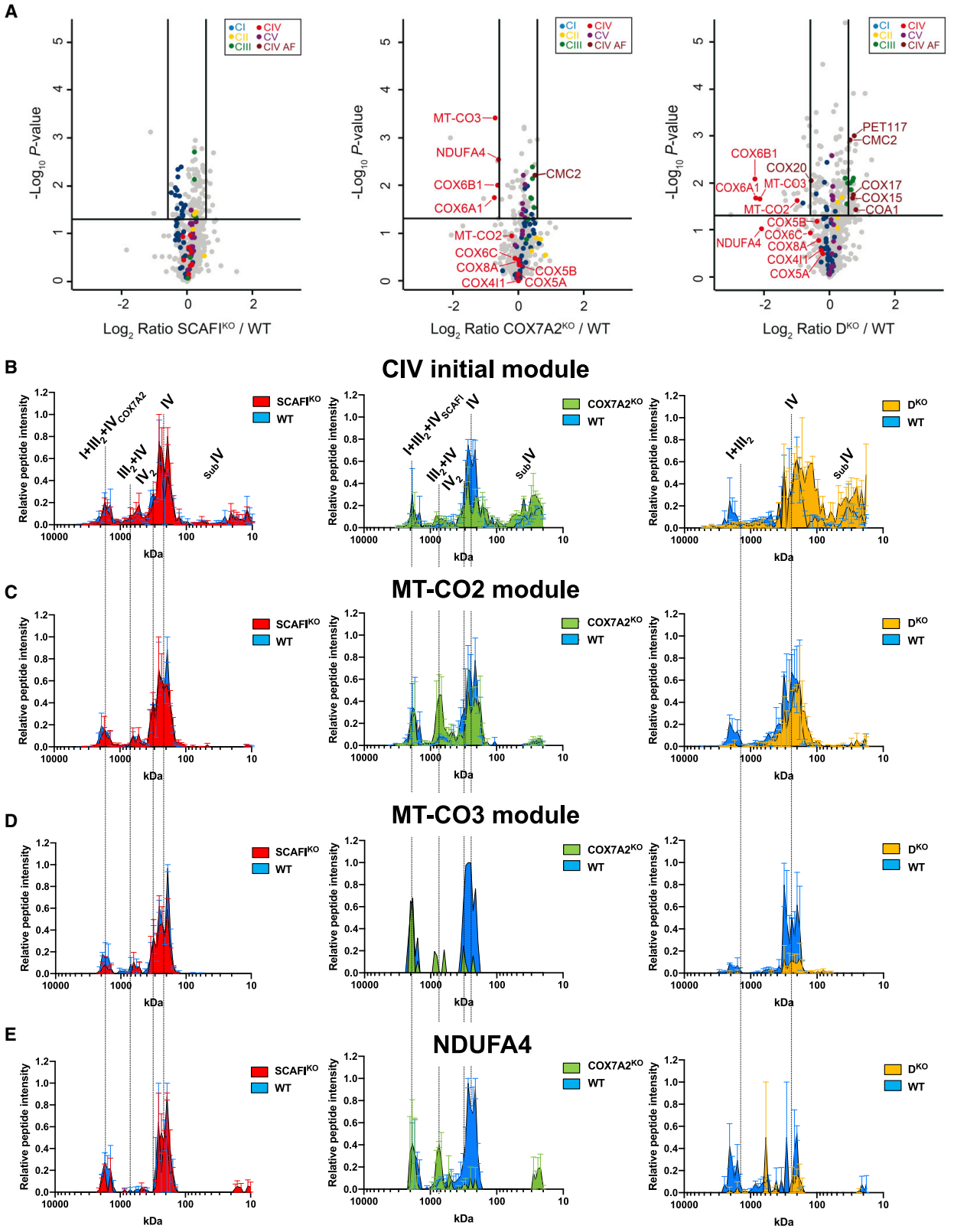

(legend on next page)

Please cite this article in press as: Fernández-Vizarra et al., Two independent respiratory chains adapt OXPHOS performance to glycolytic switch, Cell Metabolism (2022), https://doi.org/10.1016/j.cmet.2022.09.005

III_2+IV and leaves a higher proportion of $CIII_2$ in the free state (Figures 4B and 4D), similar to the situation in $SCAFI^{KO}$ cells (Figure S5B). Of note, the C-MRC organizations promoted by either COX7A1 in muscle or by COX7A2 in $SCAFI^{KO}$ cells displayed similar structural features in terms of distribution and stoichiometry of CIV subunits (Figures 2, 3B–3E, 4B, 4D, and S3A–S3C). Accordingly, overexpression of either $COX7A2^{FLAG}$ (Figures S6A and S6B) or $COX7A1^{FLAG}$ (Figures S6C and S6D) promoted the C-MRC organization by decreasing SCAFI levels, thus restoring fully assembled CIV within the C-respirasome and as a free form. Conversely, $SCAFI^{FLAG}$ overexpression (Figures S6E and S6F) restored CIV assembly in the S-MRC organization, without structurally affecting the C-MRC (Lobo-Jarne et al., 2018). These observations demonstrate that the S-MRC is reversibly modulated by the levels of COX7A1 and COX7A2 and and that in this organization, the preferential and more stable interaction of SCAFI with CIV occurs within the SCs. Overall, our analyses support the idea that the prevalence of the different CIV-containing structures in human cells and tissues depends exclusively on the predominance of the COX7A1–2 isoforms relative to SCAFI. This fact provides an explanation to why no SCAFI-containing respirasome structure has been found in mammalian tissues that robustly express COX7A1, e.g., skeletal and cardiac muscle (Vercellino and Sazanov, 2021).

Simultaneous loss of SCAFI and COX7A2 causes respiratory deficiency

To determine the functional impact of the MRC structural re-arrangements promoted by the COX7A isoforms, we first tested the proliferation of the different cell lines in high-glucose versus galactose media (Figures 5A and 5B). While glucose can be catabolized glycolytically with lactate as the final product (i.e., anaerobically), galactose forces the cells to rely on the ATP produced by OXPHOS (Bayona-Bafaluy et al., 2021). Therefore, cells with OXPHOS defects fail to proliferate in galactose medium (Robinson et al., 1992). The single KOs ($COX7A2^{KO}$ and $SCAFI^{KO}$) grew normally in glucose-containing media, but $COX7A2^{KO}$ cells grew significantly slower in galactose medium. The D^{KO} mutants showed poor growth rates in glucose and did not proliferate in galactose, similar to the "negative control" cell line lacking CIV (CIV^{KO}). In agreement, oxygen-consumption-rate (OCR) measurements in intact cells (Figure S7A) showed comparable values between $COX7A2^{KO}$, $SCAFI^{KO}$, and controls, and only the D^{KO} and CIV^{KO} cells displayed a significant respiratory defect. Polarographic measurements of the different segments of the respiratory chain in permeabilized cells, using substrates and inhibitors for each MRC complex (Figure 5C), confirmed that the origin of the respiratory defect in the D^{KO} was a strong decrease of CIV activity, with a consequent backlogging of the electronic flux through the upstream complexes. This was expected in D^{KO} cells, which had a specific CIV assembly defect (Figures 2, 3, and S3) and isolated CIV deficiency by both CIV in gel activity (IGA) (Figure S2A) and MRC spectrophotometric assays (Figure 5D). Indeed, CIV enzymatic activity significantly decreased to ~35% of the mean control value in D^{KO} cells, to ~50% in $COX7A2^{KO}$ cells, to 70% in $SCAFI^{KO}$ cells. CIV activities matched the total amounts of mature holo-CIV present in each cell line (Figure S7B), suggesting that the addition of either COX7A2 or SCAFI does not change the intrinsic functional properties of CIV. In addition, the respiration of $COX7A2^{KO}$ cells was more sensitive to inhibition with KCN (Figures 5E and 5F), confirming that the CIV defect induced by the absence of COX7A2 could not be fully compensated for by SCAFI stabilization. So why did the decrease of CIV enzymatic activity not translate into evident CIV-linked respiration defects in the $SCAFI^{KO}$ and $COX7A2^{KO}$ cells (Figure S7C)? This can be explained by the existence of a well-established "CIV excess" in human cultured cells, by which inhibition of CIV activity is not translated into reduced oxygen consumption until surpassing a specific threshold of ~50% (Villani and Attardi, 2000; Villani et al., 1998). Therefore, in basal conditions, the partial decrease in CIV activity produced by the lack of either SCAFI or COX7A2 alone would allow for normal respiration, whereas the ablation of both isoforms decreases CIV activity well below the 50% threshold, thus causing a severe respiratory decline. Despite oxygen consumption being similar in $SCAFI^{KO}$ and $COX7A2^{KO}$ (Figure 5C), the $COX7A2^{KO}$ cells were significantly more sensitive to KCN inhibition (Figure 5F). This indicates a lower reserve of COX capacity, necessary to adapt to higher metabolic demands (Villani and Attardi, 2000), which is most likely contributing to the ineffectiveness of the $COX7A2^{KO}$ cells in shifting toward OXPHOS metabolism (Figure 5A).

C-MRC is bioenergetically more efficient than S-MRC in basal conditions

To further dissect the bioenergetic properties of the two types of MRC organization, we measured the dependency of different metabolic substrates for mitochondrial respiration in cells with only C-MRC versus cells with S-MRC only ($SCAFI^{KO}$ versus $COX7A2^{KO}$ lines, respectively) (Figure 6A). The important evidence demonstrated by this set of experiments concerned the hypothesis of a compartmentalization of CoQ into two separate pools, i.e., one transferring electrons within the respirasomes and the other through the remainder MRC structures (Calvo et al., 2020; Lapuente-Brun et al., 2013). If the CoQ pools were functionally separated, in the S-MRC, where approximately half of the available $CIII_2$ is associated with the SC $I+III_2+IV_{SCAFI}$ and the other half is forming the SC III_2+IV, the NADH-linked and $FADH_2$-linked respiration would be equal, and the combination of both metabolic substrates would double the respiration of

Figure 3. Levels and distribution of CIV subunits in the C-MRC and S-MRC structural organizations

(A) Volcano plots depicting proteins with altered abundance in $SCAFI^{KO}$ (left), $COX7A2^{KO}$ (center), and D^{KO} (right) mitochondria. Significance lines were set to $p = 0.05$ and $\log_2$ ratio = 1.3.

(B–E) SILAC-CP profiles for the average of the CIV subunits belonging to different structural assembly modules as defined in the biogenetic assembly pathway of CIV (see Vidoni et al., 2017). Profiles show the relative abundance of CIV subunits in the individual peaks corresponding to the SC $I+III_2+IV_{COX7A2}$ and SC $I+III_2+IV_{SCAFI}$ (none found in the SC $I+III_2$ in the D^{KO} cells), as well as in the SC III_2+IV, CIV dimer (IV_2), and CIV monomer (IV) peaks. Left panels: comparison between WT (blue) and $SCAFI^{KO}$ (red). Center panels: WT (blue) versus $COX7A2^{KO}$ (green) cells. Right panels: WT (blue) versus $D^{KO\#8}$ cells (yellow). The values represent the mean ± SEM of duplicate SILAC-CP experiments.

Please cite this article in press as: Fernández-Vizarra et al., Two independent respiratory chains adapt OXPHOS performance to glycolytic switch, Cell Metabolism (2022), https://doi.org/10.1016/j.cmet.2022.09.005

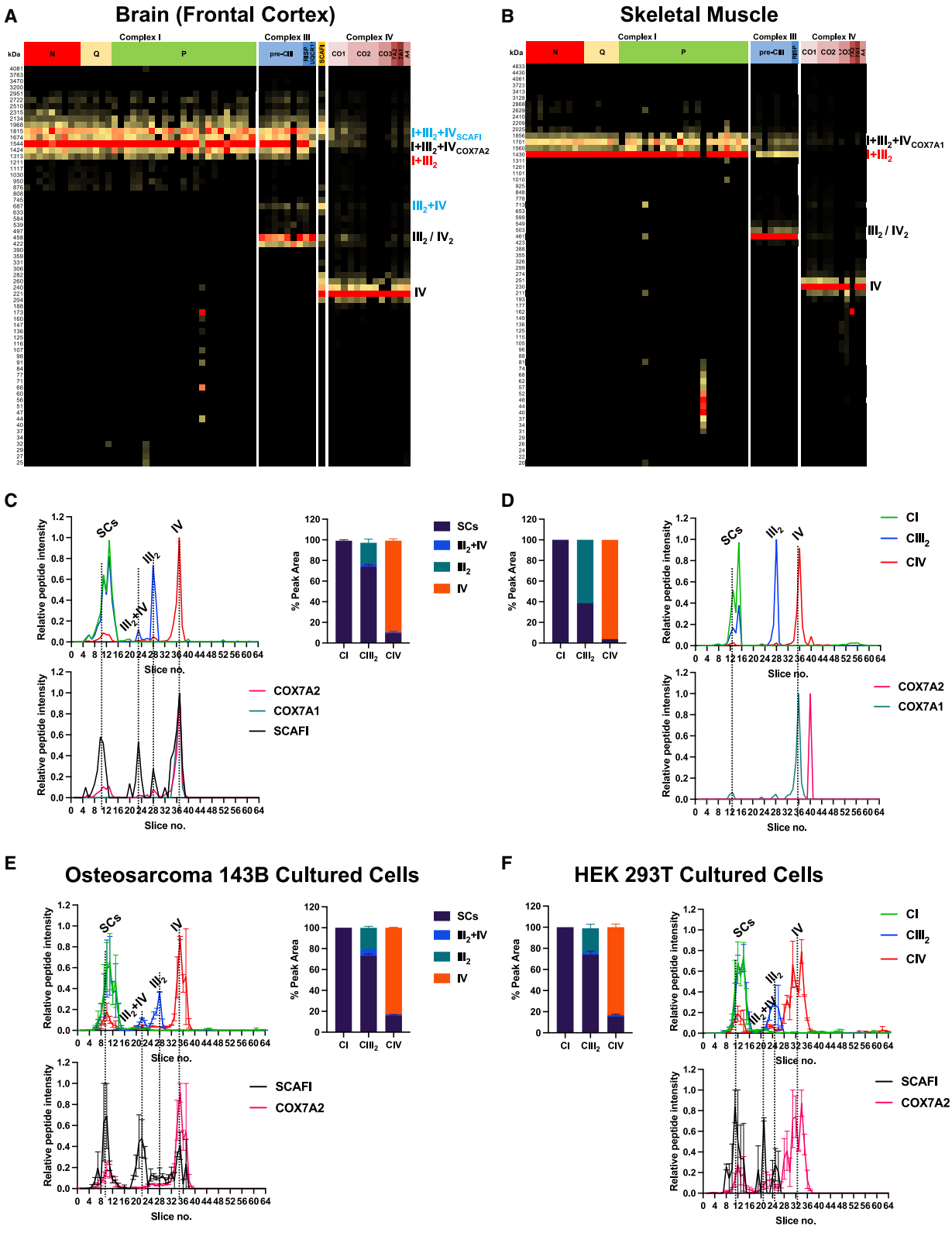

(legend on next page)

Please cite this article in press as: Fernández-Vizarra et al., Two independent respiratory chains adapt OXPHOS performance to glycolytic switch, Cell Metabolism (2022), https://doi.org/10.1016/j.cmet.2022.09.005

the individual rates. However, neither in C-MRC-only nor in S-MRC-only cell lines did we observe any evidence of compartmentalization of CoQ in two separate pools. The CI-dependent OCR levels in the presence of pyruvate-glutamate-malate (P-G-M) were comparable between the WT and the C-MRC- and S-MRC-specific cell lines cell lines (Figure 6A). The subsequent addition of succinate (S; CII-linked substrate) and glycerol-3-phosphate (G-3-P) —both donating electrons to CoQ through $FADH_2$-dependent enzymes, i.e., CII and G-3-P dehydrogenase (GPDH)—increased the respiratory rates at levels similar in all cell lines, regardless of their different MRC organizations. Importantly, the $FADH_2$-linked enzymatic rates were comparable among the cell lines regardless of whether CI was inhibited with rotenone or not. Therefore, the respiration through NADH- and $FADH_2$-dependent enzymes (including CII) together, was the same as the respiratory rate through CII alone, with no additivity of NADH- and $FADH_2$-linked substrates (Figure 6B). This result is similar to that recently reported in heart and liver mitochondria from C57BL/6 (SCAFI-less) versus CD1 (SCAFI-containing) mouse strains (Molinié et al., 2022; Mourier et al., 2014). Thus, the $FADH_2$-linked substrates alone can saturate the available CoQ as much as the combination of both types of substrates in all MRC organizations, which is consistent with the idea that electrons originating from either pathway can equally reduce all the available downstream redox centers (Blaza et al., 2014; Molinié et al., 2022). Notably, S stimulated respiration to the same extent as the combination of S + G-3-P (Figure S7D). This lack of additive effect also indicates that all $CIII_2$, regardless of whether bound to the respirasome $I+III_2+IV_{SCAFI}$ or to SC III_2+IV, can receive electrons from any reduced CoQ originating from either CI, CII, or from other $FADH_2$-dependent enzymes, such as GPDH. This observation is again compatible with the proposed free diffusion of CoQ in and out the respirasome structures (Vercellino and Sazanov, 2022). These data also support previous studies showing that electrons from mammalian CI associated into SCs can efficiently access the alternative oxidase (AOX), a monomeric enzyme that oxidizes CoQ and reduces oxygen, in submitochondrial particles (Fedor and Hirst, 2018), isolated mouse heart mitochondria (Szibor et al., 2020), and human cybrids (Protasoni et al., 2020). Interestingly, the S-MRC organization produced the most similar values between the NADH- and $FADH_2$-linked respirations (Figures 6A and 6B), meaning that the electrons from CI saturate the available downstream acceptors almost as much as those from CII and GPDH. In contrast, in the absence of SCAFI, the C-MRC produced the most divergent respiration values. This suggests that the NADH (CI) route prevails in the S-MRC, whereas the C-MRC shows a preference for the $FADH_2$ (CII) route. The choice of preferential substrate could be due to a metabolic sensing mechanism, such as that described in mouse tissue mitochondria, where the levels of the TCA cycle intermediary oxalacetate (OAA) regulate the balance between CI and CII-driven respiration (Molinié et al., 2022). Another possibility is that either electron pathway could be kinetically favored by the physical proximity of the complexes (Berndtsson et al., 2020). This phenomenon warrants further experimental investigation but, according to our data, these electronic routes would be neither exclusive nor compartmentalized.

A second important point obtained by this set of experiments is that human S-MRC displayed similar coupled and uncoupled respiratory rates to those of the C-MRC or of the mixed organization in WT cells (Figures 5C and 6A–6C). This contrasts with the proposed increase by 1 order of magnitude in the respiratory activity of the isolated Scaf1-type respirasome from mouse tissues (Calvo et al., 2020), where the co-existence of alternative respirasome species containing different Cox7a isoforms was not considered relevant. In fact, when the role of SCAFI in the compartmentalization of CoQ was originally proposed, it was assumed that all mammalian SCs were exclusively formed by SCAFI so that, in theory, in $SCAFI^{KO}$ mitochondria all CIV was free and thus completely accessible to electrons from NADH-linked and $FADH_2$-linked substrates (Lapuente-Brun et al., 2013).

Third, even though all the respiratory rates were similar in the three cell lines, the net OXPHOS capacity, i.e., the proportion of total respiratory capacity in uncoupled conditions (ETS or E) that is employed in phosphorylating respiration (OXPHOS (P) minus leak (L) respiration; Doerrier et al., 2018), was significantly lower in the $COX7A2^{KO}$ cells (Figure 6D). In addition, the "excess capacity factor" (calculated as 1 − P/E), which expresses the extent to which the OXPHOS capacity (P) is limited by the phosphorylation pathway (Doerrier et al., 2018), was significantly higher in the $COX7A2^{KO}$ cells (Figure S7E). This confirms the lower phosphorylation proficiency, in relation to the total OXPHOS capacity, of $COX7A2^{KO}$ cells compared with the WT or $SCAFI^{KO}$, in agreement with their slower proliferation in galactose medium. Overall, our data indicate that the pure S-MRC organization is bioenergetically less efficient than the C-MRC in coupling electron transfer to ATP synthesis. Notably, the increased stabilization of SCAFI in the S-MRC cannot fully compensate for the COX7A2 loss in terms of bioenergetic efficiency, even while maintaining respirasome levels similar to those in control cells. This means that the C-MRC transfers electrons more effectively downstream of the MRC, and also displays a higher energetic coupling. However, the appropriate balance of electron flow coupled with ATP production is likely

Figure 4. MRC organization in human tissues

(A and B) CP heatmaps showing the distribution and relative abundance of CI, $CIII_2$, and CIV subunits in human brain frontal cortex and skeletal muscle, respectively. Color scale is the same as in Figures 1 and 2. N, subunits belonging to the CI NADH dehydrogenase module; Q, subunits belonging to the CI CoQ-binding module; P, subunits belonging to the CI proton translocation module; Pre-CIII, subunits assembling in the early and middle stages before the incorporation of the Rieske Fe-S protein (RISP) and UQCR11; CO1, subunits belonging to the CIV initial and MT-CO1 modules; CO2, the MT-CO2 module; CO3, the MT-CO3 module; A4, peripherally associated CIV NDUFA4 subunit. Visible supercomplexes were indicated as follows: C-respirasomes, black text; S-respirasomes, blue text; SC $I+III_2$, red text; SC III_2+IV, blue text.

(C–F) CP profiles for the average of all detected CI, $CIII_2$, and CIV subunits in brain frontal cortex, skeletal muscle, osteosarcoma 143B (cybrids), and HEK 293T cells, respectively. The bar graphs depict the quantification of the relative proportion (%) of peak area corresponding to each of the species for each complex (mean ± SEM; n = 2 in brain, 143B and HEK; n = 1 in skeletal muscle). SCs: $I+III_2+$ IV and $I+III_2$; III_2+IV and individual complexes III_2 and IV.

Please cite this article in press as: Fernández-Vizarra et al., Two independent respiratory chains adapt OXPHOS performance to glycolytic switch, Cell Metabolism (2022), https://doi.org/10.1016/j.cmet.2022.09.005

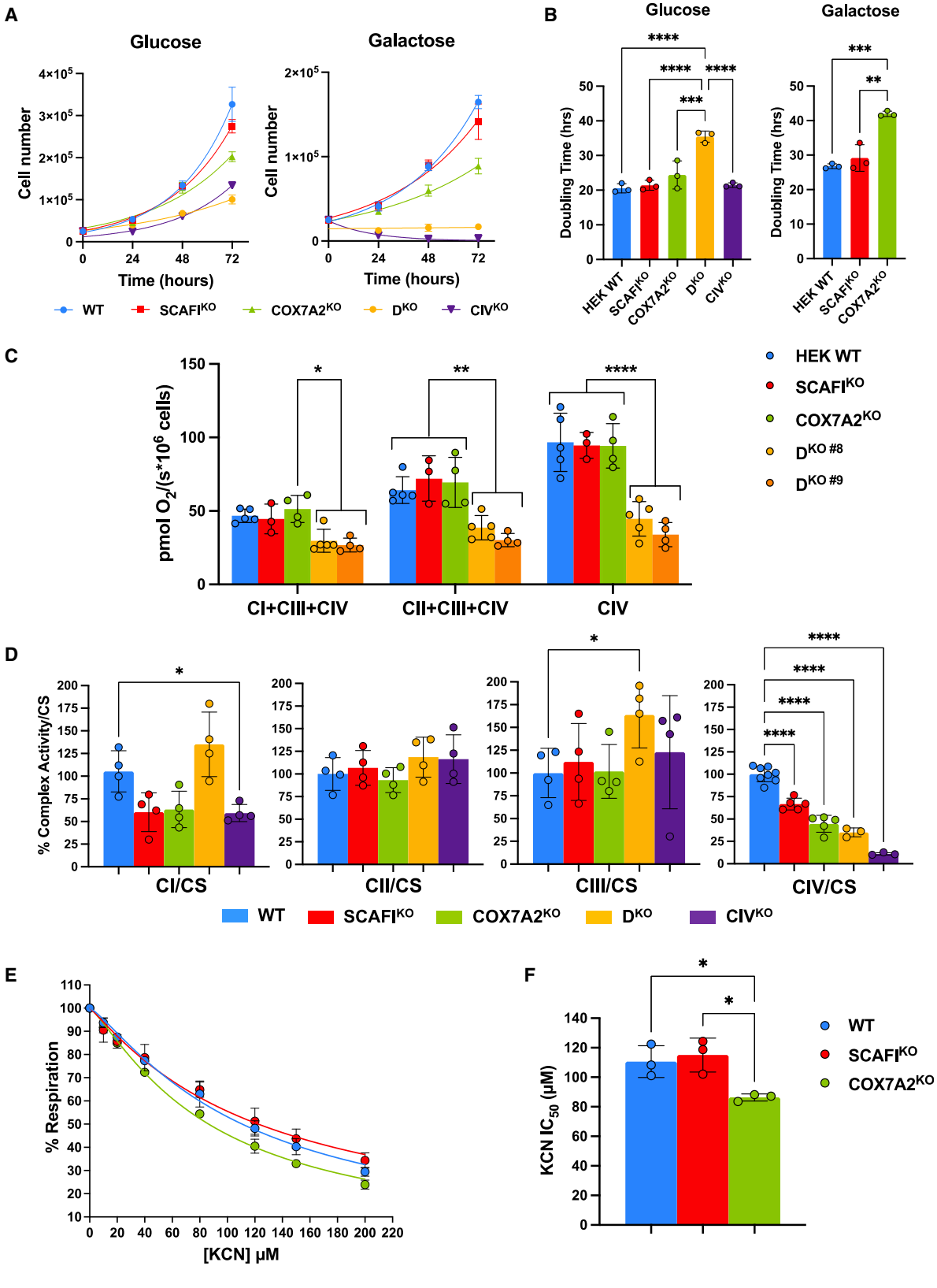

(legend on next page)

Please cite this article in press as: Fernández-Vizarra et al., Two independent respiratory chains adapt OXPHOS performance to glycolytic switch, Cell Metabolism (2022), https://doi.org/10.1016/j.cmet.2022.09.005

optimal in WT (basal) conditions, when both C-MRC and S-MRC co-exist. While our data support that the prevalent tissue-specific COX7A isoforms, COX7A2 in cultured cells and brain, and COX7A1 in muscle, are the primary structural "organizers" of the human MRC, the SCAFI-dependent adaptations in energy-transduction efficacy remain an open question.

The structural organization of the MRC is metabolically regulated by PDH activity

Emerging data have hypothesized a role of SCAFI upregulation in the adaptations of tumor cells to glycolytic metabolism, allowing them to grow in pseudohypoxic conditions (Hollinshead et al., 2020; Ikeda et al., 2019; Zhang et al., 2016). To test whether the reversible shift between glycolytic and oxidative metabolisms may modulate SCAFI levels and the structural organization of the MRC, we targeted the pyruvate dehydrogenase (PDH) enzyme activity. Cells were treated with dicholoroacetate (DCA), an inhibitor of pyruvate dehydrogenase kinase (PDK), to stimulate PDH activity by sustaining dephosphorylation of the PDHE1-alpha (PDHA) subunit. This diverts pyruvate metabolism from anaerobic lactate fermentation to the tricarboxylic acid (TCA) cycle and aerobic OXPHOS (Gray et al., 2014; Stacpoole, 2017). Remarkably, COX7A2^{KO} cells, dependent only on SCAFI, displayed significantly lower mitochondrial pyruvate consumption rates in basal conditions (Figure 7A) and were unable to adapt to the DCA-induced shift toward oxidative metabolism, showing a clear impairment in their proliferation compared with the SCAFI^{KO} and WT cell lines (Figures 7B and 7C). In fact, SCAFI levels decreased by ca. 40% of the non-treated WT and COX7A2^{KO} cells upon efficient DCA treatment leading to PDHA dephosphorylation (Figure 7D). This was accompanied by the progressive disappearance of the S-MRC organization, the stabilization of the C-MRC organization promoted by COX7A2 (Figure 7E), and the specific increase of CIV activity only in WT and SCAFI^{KO} cells (Figure 7F). Therefore, PDH activation promotes oxidative metabolism through the enhancement of the C-MRC organization in HEK cells, consequently leading to decreased SCAFI levels and S-MRC loss.

According to this hypothesis, the S-MRC formation should be predominant under conditions that promote glycolytic metabolism. To test this, we used primary skin fibroblasts from three pediatric/neonatal controls and patients with PDH deficiency associated with different mutations in the *PDHA1* (E1 alpha subunit) gene. Cells with defective PDH activity constitute a pathophysiological model of conditions, such as mitochondrial disorders, in which metabolism is shifted toward glycolysis instead of OXPHOS (Anwar et al., 2021). As shown in Figure 7G, SCAFI steady-state levels were significantly increased in the PDH-deficient fibroblasts when compared with the controls, with SCAFI accumulating mainly within the S-respirasome (Figure S7F). Moreover, the reduction of SCAFI levels by DCA treatment was significant in primary control fibroblasts but absent in the PDH-deficient cells (Figure 7H). Notably, in human fibroblasts, SCAFI is mostly associated with the respirasome species (Figure 7I). The DCA-induced decrease in SCAFI abundance observed in control primary fibroblasts was again associated with a loss of the SCAFI-containing structures and a stabilization of the C-MRC via an increase in the levels and activity of free CIV (Figure 7I). These results demonstrate for the first time in independent cellular models that the structural and functional organization of the respiratory chain is directly modulated by the enzymatic activity of the PDH complex. And also, that the S-MRC is the preferential structural organization in cells operating predominantly on glycolysis, whereas the C-MRC is favored in OXPHOS-dependent metabolic settings.

Importantly, our data show the direct connection between the different metabolic signatures converging at the PDH complex and the structural and functional organization of the MRC, in which the COX7A isoforms play a central role. Inhibition of PDH activity triggers a switch toward a glycolytic metabolism that induces SCAFI stabilization most likely to favor a bioenergetic adaptation through the S-MRC, which is less efficient in coupling respiration with ATP synthesis. Therefore, the S-MRC organization promoted by SCAFI would be essential for the adaptation toward anaerobic ATP synthesis via glycolysis and lactic fermentation. Conversely, forcing the cells to use oxidative metabolism through PDH activation mechanisms would favor energetic fitness through the C-MRC, in detriment of the SCAFI-dependent S-MRC organization. Accordingly, SCAFI^{KO} cells (only expressing COX7A2) metabolize pyruvate at normal rates and are able to adapt completely to PDH activation, whereas COX7A2^{KO} cells (only expressing SCAFI) are unable to efficiently adapt to the switch to oxidative metabolism. These observations offer a straightforward explanation to the contribution of SCAFI to hypoxia tolerance in tumor environments and tumor growth (Zhang et al., 2016). Moreover, SCAFI expression is upregulated as a consequence of endoplasmic reticulum (ER) stress activation via the PERK-eIF2α-ATF4 axis (Balsa et al.,

Figure 5. Simultaneous loss of COX7A2 and SCAFI leads to isolated complex IV deficiency

(A) Effects of COX7A2 and SCAFI absence on cell growth. Cells were cultured in media containing either 25 mM glucose (left) or 10 mM galactose (right) on P6 plates at 5 × 10^4 cells per plate and counted on a daily basis for 72 h. Data points represent mean ± SD values from 6 to 9 experimental replicates.

(B) Doubling times (DT) were calculated from the cell growth curves in (A). The DTs of the D^{KO} and CIV^{KO} cell lines in galactose were not determined (nd) as these cells do not proliferate in that medium.

(C) Polarography analysis in digitonin-permeabilized cells. CI+CIII+CIV OCRs were measured after adding ADP + Pi to the medium and 10 mM glutamate and 2 mM malate. CII+CIII+CIV OCRs were measured after adding 1 μM rotenone, 10 mM succinate, and 10 mM glycerol-3-phosphate (G-3-P). CIV OCRs were measured after adding 2 μM antimycin A, 2 mM ascorbate, and 1 mM TMPD. CIV was inhibited by adding 1.5 mM KCN. Graphs represent the mean ± SD of 3–5 independent measurements; *p < 0.05, **p < 0.01, and ****p < 0.0001, one-way or two-way ANOVA with Tukey's multiple comparisons test.

(D) MRC enzymatic activities normalized by citrate synthase (CS). Plotted values represent the mean ± SD of 4–8 biological replicates each measured in duplicate; *p < 0.05 and ****p < 0.0001 two-way ANOVA with Tukey's multiple comparisons test.

(E) % OCR versus KCN concentration to determine sensitivity to CIV inhibition. Plotted values are the mean ± SD of three independent experiments, adjusted to a two-slope inhibition curve.

(F) KCN IC_{50} values calculated from the inhibition curves for each independent experiment. The graph shows the mean ± SD, *p < 0.05 one-way ANOVA with Tukey's multiple comparisons test. In all graphs, individual data points are shown with overlaying dot plots.

Please cite this article in press as: Fernández-Vizarra et al., Two independent respiratory chains adapt OXPHOS performance to glycolytic switch, Cell Metabolism (2022), https://doi.org/10.1016/j.cmet.2022.09.005

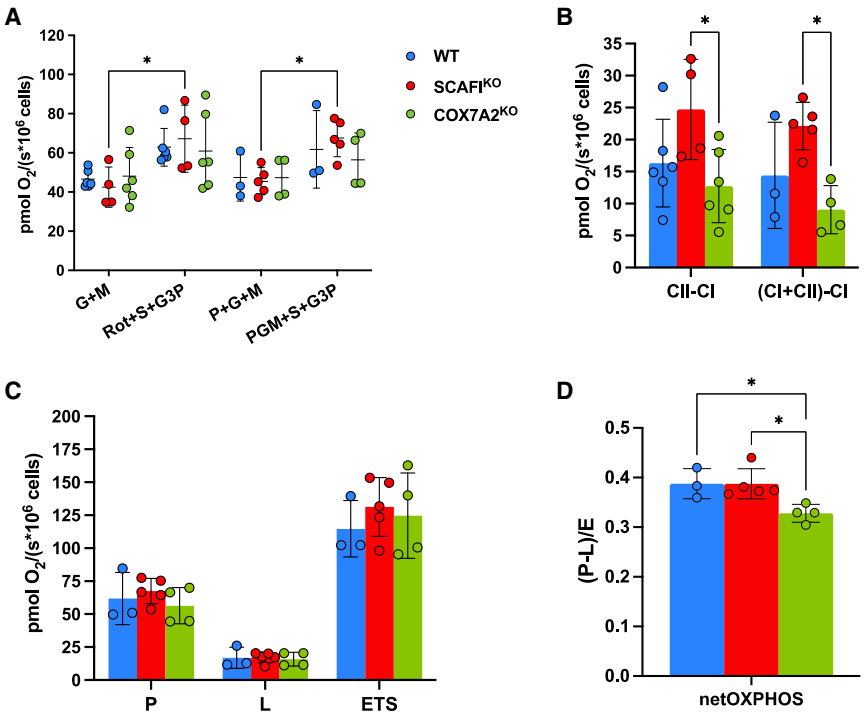

Figure 6. C-MRC is bioenergetically more efficient than S-MRC

(A) High resolution respirometry in permeabilized cells in the presence of the indicated substrate-inhibitor combinations. G, glutamate; M, malate; Rot, rotenone; S, succinate; G3P, glycerol-3-phosphate.

(B) Differential respiration rates, "CII-CI" was calculated by subtracting the Rot+S+G3P from the G+M OCR values (from A). The "(CI+CII)-CI" was calculated by subtracting the PGM+S+G3P from the P+G+M OCR values from (A).

(C) Respiratory rates in permeabilized cells. Basal phosphorylating respiration or OXPHOS state (P) represent the ones in (A) (PGM+S+G3P in the presence of saturating concentrations of ADP). Non-phosphorylating OCRs (leak, L) were measured with 2.5 μM of the ATP synthase inhibitor oligomycin. Maximal or total respiratory capacity (ETS) was measured as the uncoupled respiration obtained by CCCP titration until reaching maximal respiration rates (see Figure S7D).

(D) For each cell line, the net phosphorylating capacity of the OXPHOS system (netOXPHOS), expressed as a fraction of the total respiratory capacity, was calculated by subtracting the L respiration from the P rates and dividing this value by the ETS ([P–L]/E), data from (C), see main text for more details.

For (A)–(D), error bars represent the mean ± SD of 3–6 independent measurements; *p ≤ 0.05 two-way ANOVA with Tukey's multiple comparisons test. In all graphs, individual data points are shown with overlaying dot plots.

2019), the same signaling pathway that is elicited by the down-regulation of the COX7A subunit in *Drosophila*, where it promotes a metabolic shift toward glycolysis, thus increasing oncogenic activity via the Warburg effect (Sorge et al., 2020). Interestingly, targeting PDH activity with DCA has been proposed as a therapeutic strategy for cancer, but DCA treatment seems to work more efficiently in tumor cells with a glycolytic profile than in those with an oxidative metabolism, which become resistant (Tataranni et al., 2019). This is in line with the differential effects of DCA observed in the OXPHOS-proficient SCAFI^{KO} cells, which are able to proliferate in the presence of DCA, whereas the less OXPHOS-efficient COX7A^{KO} cells failed to grow in these conditions and were unable to adapt their CIV enzymatic activity to the higher OXPHOS demand. In summary, our work evidences a direct link between the regulation of pyruvate metabolism (Echeverri Ruiz et al., 2021; Schell et al., 2014, 2017) and the structural and functional organization of the MRC. Our data now answer the fundamental question concerning the physiological relevance of the interplay between the different COX7A isoforms in metabolic regulation, highlighting the pathophysiological role of SCAFI in metabolic disorders and cancer and the exciting possibility of targeting the PDH-SCAFI axis for future therapeutic approaches.

Limitations of study

The main limitation of our work is that we have examined the functions of COX7A proteins in cultured cells and under standard conditions, which has, however, unveiled new mechanisms and pathways regulating the reorganization of the MRCs under varying metabolic conditions. It is therefore necessary to extend these studies using appropriate animal models in which to analyze the pathophysiological consequences of modulating the genetic expression of the different COX7A isoforms in a tissue-specific manner, as well as their potential metabolic regulation *in vivo* through the different cell-signaling mechanisms converging at the PDC.

Concluding remarks

The functional concurrence of diverse COX7A isoforms constitutes a redundant regulatory mechanism to prevent MRC deficiency and takes place by promoting alternative organizations of the MRC complexes I, III, and IV, with differential biogenetical and bioenergetic properties, that co-exist in normal cells and tissues. Notably, the S-MRC is unable to fully compensate for the absence of COX7A2 in terms of bioenergetic efficiency, even while maintaining similar respirasome levels as in control cells. This means that the C-MRC couples electron transfer with ATP production more effectively throughout the MRC, thus displaying a higher energetic coupling. However, we propose that the optimal conditions for metabolic adaptation likely take place in the WT conditions, i.e., when both C-MRC and S-MRC are in play. While our data support that the prevalent tissue-specific COX7A isoforms, COX7A2 in cultured cells and brain, and COX7A1 in skeletal muscle, are the primary structural organizers of the human MRC, the SCAFI-dependent adaptations in energy-transduction efficacy become relevant in metabolic contexts that promote a glycolytic switch.

Please cite this article in press as: Fernández-Vizarra et al., Two independent respiratory chains adapt OXPHOS performance to glycolytic switch, Cell Metabolism (2022), https://doi.org/10.1016/j.cmet.2022.09.005

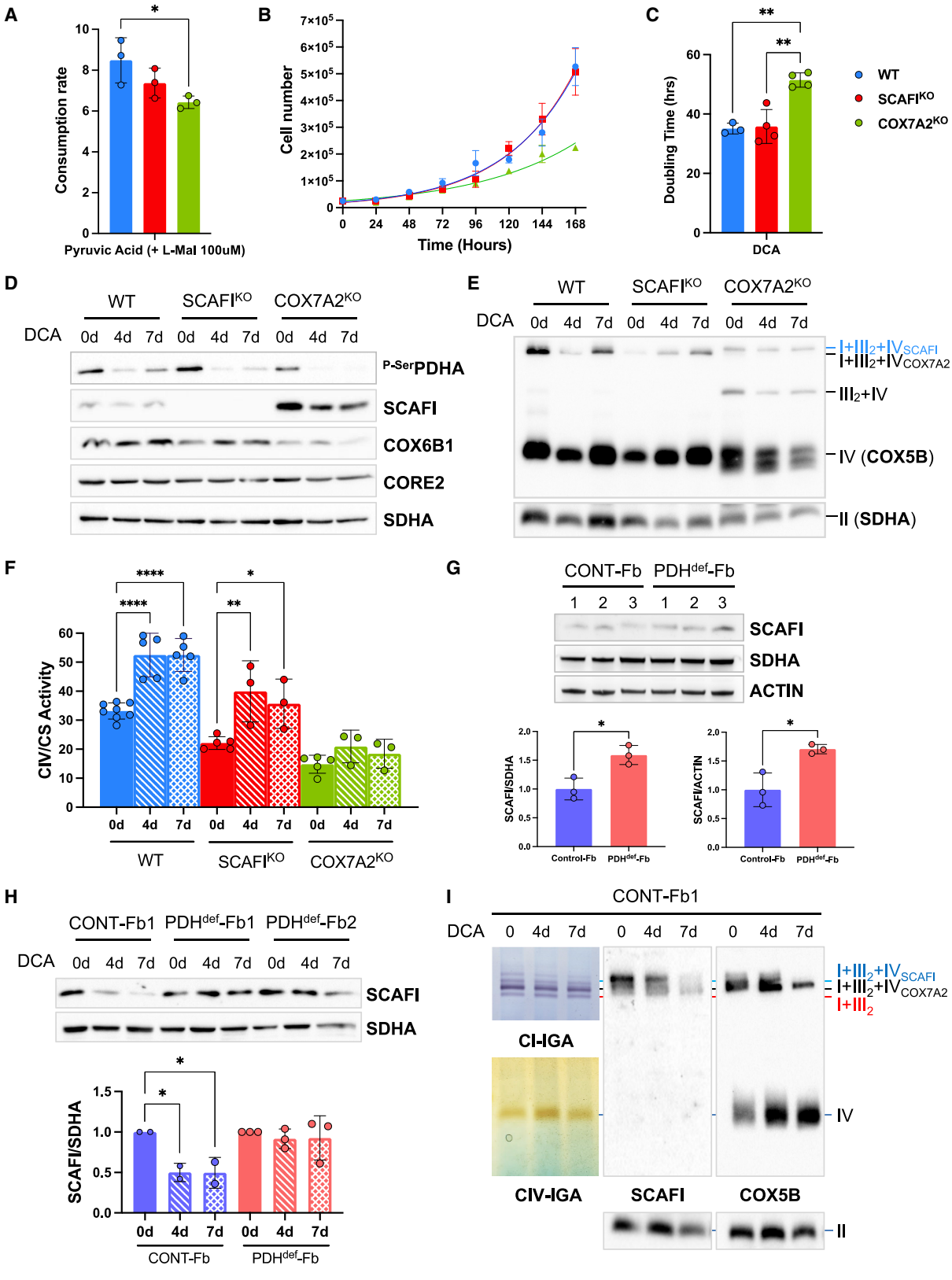

(legend on next page)

Please cite this article in press as: Fernández-Vizarra et al., Two independent respiratory chains adapt OXPHOS performance to glycolytic switch, Cell Metabolism (2022), https://doi.org/10.1016/j.cmet.2022.09.005

Overall, our results open new perspectives for understanding the structural and functional organization of the MRC, and clarify the roles played by the COX7A isoforms in this process. The precise determination of each of the heterogeneous human SC structures will definitively help unveil the molecular mechanisms by which COX7A-mediated CIV binding may modulate their different functional properties.

STAR★METHODS

Detailed methods are provided in the online version of this paper and include the following:

- KEY RESOURCES TABLE
- RESOURCE AVAILABILITY
  - Lead contact
  - Materials availability
  - Data and code availability
- EXPERIMENTAL MODEL AND SUBJECT DETAILS
  - Human cell lines and primary fibroblasts
  - Human tissues
- METHOD DETAILS
  - Cell culture
  - Gene editing and Screening
  - Real time quantitative PCR
  - Cell growth
  - Respirometry
  - Protein separation by SDS-PAGE and Immunoblotting
  - Blue Native Electrophoresis and In-Gel Activity Assays
  - Antibody detection
  - Acquisition and analysis of mass spectrometry data from HEK293T cells
  - Complexome Profiling
  - Measurement of pyruvate consumption rates
- QUANTIFICATION AND STATISTICAL ANALYSIS

SUPPLEMENTAL INFORMATION

Supplemental information can be found online at https://doi.org/10.1016/j.cmet.2022.09.005.

ACKNOWLEDGMENTS

We thank all lab members for constructive discussions and M.E. Harbour and P. Páleníková (University of Cambridge) for their help with the CP datasets. We thank E. Lamantea and the biobank "Cell line and DNA Bank of Genetic Movement Disorders and Mitochondrial Diseases," member of the Telethon Network of Genetic Biobanks (project no. GTB12001), funded by Telethon Italy and the EuroBioBank network, for the PDH-deficient fibroblasts. We thank M.G. Hanna, co-lead for the London NHS England Highly Specialised Service for Rare Mitochondrial Disorders, for access to patient-derived tissue. We are grateful to A. Sanz and K. Tokatlidis (University of Glasgow) and C. Viscomi and T. Calì (University of Padova) for their support, as well as to C. Romualdi (University of Padova) and C. Doerrier (Oroboros Instruments) for insightful revision and discussions about the respirometry datasets. Research was funded by Instituto de Salud Carlos III-MINECO/European FEDER Funds grants PI17-00048, PI20-00057 (to C.U.), and PI18-01374 (to M.A.M.); by Comunidad Autónoma de Madrid/ERDF-ESF grant S2018/BAA-4403 (to C.U.); by Association Française contre les Myopathies (AFM) grant 16086 (to E.F.-V.); by Fondazione Telethon-Cariplo grant GJC21014 (to E.F.-V.); by Research Council of Norway (288164), Bergen Research Foundation (BFS2017REK05), and Western Norway Regional Health Authority (F-11470) (to C.T.); by a Clinician Scientist Fellowship (MR/S002065/1) and Strategic Award (MR/S005021/1) from Medical Research Council (MRC, UK) (to R.D.S.P.); by a Core Grant from MRC (MC_UU_00015/5), an Advanced Grant from the European Research Council (ERC) (MITCARE: FP7-322424), Mitofight Grant—Associazione Renato Comini Onlus, and NRJ Institut de France Grant (to M.Z.); and by the Australian National Health and Medical Research Council (NHMRC project grants #1165217 and #1164459 to M.T.R., #1125390 and #1140906 to D.A.S. and M.T.R., and NHMRC Fellowship 1140851 to D.A.S.). D.H.H. is supported by a Melbourne International Research Scholarship and Mito Foundation (incorporated as Australian Mitochondrial Disease Foundation) Top-up Scholarship. We acknowledge support from the Bio21 Mass Spectrometry and Proteomics Facility (MMSPF) for the provision of instrumentation, training, and technical support, and the Mito Foundation for the provision of instrumentation.

Figure 7. Regulation of MRC organization by pyruvate dehydrogenase activity

(A) Rates of pyruvate utilization by the mitochondria of WT, SCAFI^{KO}, and COX7A2^{KO} cells measured in triplicate using the Biolog MitoPlate S1 system. Error bars represent the mean ± SD; *p < 0.05 one-way ANOVA with Tukey's multiple comparisons test.

(B) Cell growth in the presence of dicloroacetate (DCA). Cells were cultured in glucose media containing 30 mM of DCA on P6 plates at 5 × 10^4 cells per plate and counted on a daily basis for up to 168 h. Data points represent mean ± SD values from 4 to 8 independent replicates.

(C) Doubling times (DTs) were calculated adjusting the cell growth curves in (B) to an exponential growth equation.

(D) Immunodetection of total PDHA, phosphorylated PDHA ($^{P\text{-}Ser}$PDHA), SCAFI, COX6B1 (CIV), CORE2 ($CIII_2$), and SDHA (loading control) on western blot of mitochondrial extracts from cells treated with DCA for 0, 4, and 7 days and separated by SDS-PAGE.

(E) BN-PAGE by western blot and immunodetection (lower panels) of isolated mitochondria from DCA-treated cells treated solubilized with 4 mg digitonin/mg protein using antibodies raised against COX5B (CIV) and SDHA (CII). The bands corresponding to the different CIV-containing species, i.e., the two respirasome types ($I+III_2+IV_{SCAFI}$ and $I+III_2+IV_{COX7A2}$), SC III_2+IV, and individual CIV are indicated.

(F) Cytochrome *c* oxidase (CIV) enzymatic activity normalized by citrate synthase (CS) activity in DCA-treated cells. Plotted values represent the mean ± SD of three to eight biological replicates each measured in duplicate. **p < 0.01, ***p < 0.001, and ****p < 0.0001 one-way ANOVA with Tukey's multiple comparisons test.

(G) Immunodetection of SCAFI and SDHA and actin (cytoplasmic and mitochondrial loading controls, respectively) on western blot of total lysates from primary skin fibroblasts from three patients carrying mutations in *PDHA1* (PDH^{def}-Fb) and three different controls (CONTROL-Fb), separated by SDS-PAGE. The graph represents the mean ± SD of the densitometric quantification of the SCAFI signals normalized to either SDHA or actin in duplicate independent experiments. *p < 0.05, **p < 0.01, unpaired Student's t test.

(H) Representative immunodetection of SCAFI and SDHA (loading control) on western blot of mitochondria from primary fibroblasts (one control and two PDH^{def} patients) treated with DCA for the indicated time points in days and separated by SDS-PAGE. The graph represents the mean ± SD of the densitometric quantification of the normalized SCAFI band signals from two independent control and three patient fibroblast lines measured in duplicate independent experiments. For internal comparison, the values at time 0 days were set as 1 in all cases. *p < 0.05 one-way ANOVA with Dunett's multiple comparisons test.

(I) BN-PAGE followed by CI- and CIV-in gel activity (IGA) and by western blot and immunodetection (right panels) of isolated mitochondria from primary control fibroblasts treated with DCA for 0, 4, and 7 days, solubilized with 4 mg digitonin/mg protein using antibodies raised against SCAFI, COX5B (CIV), and SDHA (CII). The bands corresponding to the different CIV-containing species, i.e., the two respirasome types ($I+III_2+IV_{SCAFI}$ and $I+III_2+IV_{COX7A2}$), as well as SC $I+III_2$ and individual CIV are indicated. In all bar graphs, individual data points are shown with overlaying dot plots.

AUTHOR CONTRIBUTIONS

Conceptualization, E.F.-V. and C.U.; methodology, E.F.-V., S.L.-C., A.S.-M., R.P.-P., L.E.F., D.H.H., M.I., A.P., M.B., S.D., I.M.F., C.T., R.D.S.P., M.A.M., D.A.S., M.Z., M.T.R., and C.U.; formal analysis, E.F.-V., S.L.-C., A.S.-M., R.P.-P., L.E.F., D.H.H., M.I., A.P., M.B., S.D., I.M.F., D.A.S., M.T.R., and C.U.; investigation, E.F.-V., S.L.-C., A.S.-M., R.P.-P., L.E.F., D.H.H., M.I., A.P., M.B., and C.U.; data curation, E.F.-V., S.L.-C., A.S.-M., R.P.-P., L.E.F., D.A.S., M.Z., M.T.R., and C.U.; writing – original draft, E.F.-V. and C.U.; writing – review & editing, E.F.-V., S.L.-C., A.S.-M., R.P.-P., L.E.F., D.H.H., M.I., A.P., S.D., I.M.F., C.T., R.D.S.P., J.A., M.A.M., D.A.S., M.Z., M.T.R., and C.U.; visualization, E.F.-V. and C.U.; supervision, E.F.-V., C.T., R.D.S.P., J.A., M.A.M., D.A.S., M.Z., M.T.R., and C.U.; project administration, E.F.-V., J.A., M.A.M., D.A.S., M.Z., M.T.R., and C.U.; funding acquisition, E.F.-V., C.T., R.D.S.P., M.A.M., D.A.S., M.Z., M.T.R., and C.U.

DECLARATION OF INTERESTS

The authors declare no competing interests.

Received: February 22, 2021
Revised: June 21, 2022
Accepted: September 8, 2022
Published: October 4, 2022

REFERENCES

Acín-Pérez, R., Fernández-Silva, P., Peleato, M.L., Pérez-Martos, A., and Enriquez, J.A. (2008). Respiratory active mitochondrial supercomplexes. Mol. Cell *32*, 529–539. https://doi.org/10.1016/j.molcel.2008.10.021.

Anwar, S., Shamsi, A., Mohammad, T., Islam, A., and Hassan, M.I. (2021). Targeting pyruvate dehydrogenase kinase signaling in the development of effective cancer therapy. Biochim. Biophys. Acta Rev. Cancer *1876*, 188568. https://doi.org/10.1016/j.bbcan.2021.188568.

Balsa, E., Soustek, M.S., Thomas, A., Cogliati, S., García-Poyatos, C., Martín-García, E., Jedrychowski, M., Gygi, S.P., Enriquez, J.A., and Puigserver, P. (2019). ER and nutrient stress promote assembly of respiratory chain supercomplexes through the PERK-eIF2alpha axis. Mol. Cell *74*, 877–890.e6. https://doi.org/10.1016/j.molcel.2019.03.031.

Bayona-Bafaluy, M.P., Montoya, J., and Ruiz-Pesini, E. (2021). Oxidative phosphorylation system and cell culture media. Trends Cell Biol. *31*, 618–620. https://doi.org/10.1016/j.tcb.2021.05.003.

Berndtsson, J., Aufschnaiter, A., Rathore, S., Marin-Buera, L., Dawitz, H., Diessl, J., Kohler, V., Barrientos, A., Büttner, S., Fontanesi, F., and Ott, M. (2020). Respiratory supercomplexes enhance electron transport by decreasing cytochrome c diffusion distance. EMBO Rep. *21*, e51015. https://doi.org/10.15252/embr.202051015.

Bianchi, C., Genova, M.L., Parenti Castelli, G., and Lenaz, G. (2004). The mitochondrial respiratory chain is partially organized in a supercomplex assembly: kinetic evidence using flux control analysis. J. Biol. Chem. *279*, 36562–36569. https://doi.org/10.1074/jbc.M405135200.

Blaza, J.N., Serreli, R., Jones, A.J., Mohammed, K., and Hirst, J. (2014). Kinetic evidence against partitioning of the ubiquinone pool and the catalytic relevance of respiratory-chain supercomplexes. Proc. Natl. Acad. Sci. USA *111*, 15735–15740. https://doi.org/10.1073/pnas.1413855111.

Calvo, S.E., Clauser, K.R., and Mootha, V.K. (2016). MitoCarta2.0: an updated inventory of mammalian mitochondrial proteins. Nucleic Acids Res. *44*, D1251–D1257. https://doi.org/10.1093/nar/gkv1003.

Calvo, E., Cogliati, S., Hernansanz-Agustín, P., Loureiro-López, M., Guarás, A., Casuso, R.A., García-Marqués, F., Acín-Pérez, R., Martí-Mateos, Y., Silla-Castro, J.C., et al. (2020). Functional role of respiratory supercomplexes in mice: SCAF1 relevance and segmentation of the Q pool. Sci. Adv. *6*, eaba7509. https://doi.org/10.1126/sciadv.aba7509.

Cogliati, S., Calvo, E., Loureiro, M., Guaras, A.M., Nieto-Arellano, R., Garcia-Poyatos, C., Ezkurdia, I., Mercader, N., Vázquez, J., and Enriquez, J.A. (2016). Mechanism of super-assembly of respiratory complexes III and IV. Nature *539*, 579–582. https://doi.org/10.1038/nature20157.

Cogliati, S., Cabrera-Alarcón, J.L., and Enriquez, J.A. (2021). Regulation and functional role of the electron transport chain supercomplexes. Biochem. Soc. Trans. *49*, 2655–2668. https://doi.org/10.1042/BST20210460.

Cox, J., and Mann, M. (2008). MaxQuant enables high peptide identification rates, individualized p.p.b.-range mass accuracies and proteome-wide protein quantification. Nat. Biotechnol. *26*, 1367–1372. https://doi.org/10.1038/nbt.1511.

Cruciat, C.M., Brunner, S., Baumann, F., Neupert, W., and Stuart, R.A. (2000). The cytochrome bc1 and cytochrome c oxidase complexes associate to form a single supracomplex in yeast mitochondria. J. Biol. Chem. *275*, 18093–18098. https://doi.org/10.1074/jbc.M001901200.

Doerrier, C., Garcia-Souza, L.F., Krumschnabel, G., Wohlfarter, Y., Mészáros, A.T., and Gnaiger, E. (2018). High-resolution FluoRespirometry and OXPHOS protocols for human cells, permeabilized fibers from small biopsies of muscle, and isolated mitochondria. Methods Mol. Biol. *1782*, 31–70. https://doi.org/10.1007/978-1-4939-7831-1_3.

Echeverri Ruiz, N.P., Mohan, V., Wu, J., Scott, S., Kreamer, M., Benej, M., Golias, T., Papandreou, I., and Denko, N.C. (2021). Dynamic regulation of mitochondrial pyruvate metabolism is necessary for orthotopic pancreatic tumor growth. Cancer Metab. *9*, 39. https://doi.org/10.1186/s40170-021-00275-4.

Fang, H., Ye, X., Xie, J., Li, Y., Li, H., Bao, X., Yang, Y., Lin, Z., Jia, M., Han, Q., et al. (2021). A membrane arm of mitochondrial complex I sufficient to promote respirasome formation. Cell Rep. *35*, 108963. https://doi.org/10.1016/j.celrep.2021.108963.

Fedor, J.G., and Hirst, J. (2018). Mitochondrial supercomplexes do not enhance catalysis by quinone channeling. Cell Metab. *28*, 525–531.e4. https://doi.org/10.1016/j.cmet.2018.05.024.

Fernández-Vizarra, E., and Ugalde, C. (2022). Cooperative assembly of the mitochondrial respiratory chain. Trends Biochem. Sci. https://doi.org/10.1016/j.tibs.2022.07.005.

Fernández-Vizarra, E., López-Calcerrada, S., Formosa, L.E., Pérez-Pérez, R., Ding, S., Fearnley, I.M., Arenas, J., Martín, M.A., Zeviani, M., Ryan, M.T., and Ugalde, C. (2021). SILAC-based complexome profiling dissects the structural organization of the human respiratory supercomplexes in SCAF1^{KO} cells. Biochim. Biophys. Acta Bioenerg. *1862*, 148414. https://doi.org/10.1016/j.bbabio.2021.148414.

García-Poyatos, C., Cogliati, S., Calvo, E., Hernansanz-Agustín, P., Lagarrigue, S., Magni, R., Botos, M., Langa, X., Amati, F., Vázquez, J., et al. (2020). Scaf1 promotes respiratory supercomplexes and metabolic efficiency in zebrafish. EMBO Rep. *21*, e50287. https://doi.org/10.15252/embr.202050287.

Gray, L.R., Tompkins, S.C., and Taylor, E.B. (2014). Regulation of pyruvate metabolism and human disease. Cell. Mol. Life Sci. *71*, 2577–2604. https://doi.org/10.1007/s00018-013-1539-2.

Gu, J., Wu, M., Guo, R., Yan, K., Lei, J., Gao, N., and Yang, M. (2016). The architecture of the mammalian respirasome. Nature *537*, 639–643. https://doi.org/10.1038/nature19359.

Guo, R., Zong, S., Wu, M., Gu, J., and Yang, M. (2017). Architecture of human mitochondrial respiratory megacomplex $I_2III_2IV_2$. Cell *170*, 1247–1257.e12. https://doi.org/10.1016/j.cell.2017.07.050.

Hirst, J. (2018). Open questions: respiratory chain supercomplexes-why are they there and what do they do? BMC Biol. *16*, 111. https://doi.org/10.1186/s12915-018-0577-5.

Hock, D.H., Reljic, B., Ang, C.S., Muellner-Wong, L., Mountford, H.S., Compton, A.G., Ryan, M.T., Thorburn, D.R., and Stroud, D.A. (2020). HIGD2A is required for assembly of the COX3 module of human mitochondrial complex IV. Mol. Cell. Proteomics *19*, 1145–1160. https://doi.org/10.1074/mcp.RA120.002076.

Hofhaus, G., Shakeley, R.M., and Attardi, G. (1996). Use of polarography to detect respiration defects in cell cultures. Methods Enzymol. *264*, 476–483. https://doi.org/10.1016/s0076-6879(96)64043-9.

Hollinshead, K.E.R., Parker, S.J., Eapen, V.V., Encarnacion-Rosado, J., Sohn, A., Oncu, T., Cammer, M., Mancias, J.D., and Kimmelman, A.C. (2020). Respiratory supercomplexes promote mitochondrial efficiency and growth in

severely hypoxic pancreatic cancer. Cell Rep. *33*, 108231. https://doi.org/10.1016/j.celrep.2020.108231.

Ikeda, K., Shiba, S., Horie-Inoue, K., Shimokata, K., and Inoue, S. (2013). A stabilizing factor for mitochondrial respiratory supercomplex assembly regulates energy metabolism in muscle. Nat. Commun. *4*, 2147. https://doi.org/10.1038/ncomms3147.

Ikeda, K., Horie-Inoue, K., Suzuki, T., Hobo, R., Nakasato, N., Takeda, S., and Inoue, S. (2019). Mitochondrial supercomplex assembly promotes breast and endometrial tumorigenesis by metabolic alterations and enhanced hypoxia tolerance. Nat. Commun. *10*, 4108. https://doi.org/10.1038/s41467-019-12124-6.

Javadov, S., Jang, S., Chapa-Dubocq, X.R., Khuchua, Z., and Camara, A.K. (2021). Mitochondrial respiratory supercomplexes in mammalian cells: structural versus functional role. J. Mol. Med. (Berl) *99*, 57–73. https://doi.org/10.1007/s00109-020-02004-8.

Labun, K., Montague, T.G., Gagnon, J.A., Thyme, S.B., and Valen, E. (2016). CHOPCHOP v2: a web tool for the next generation of CRISPR genome engineering. Nucleic Acids Res. *44*, W272–W276. https://doi.org/10.1093/nar/gkw398.

Lapuente-Brun, E., Moreno-Loshuertos, R., Acín-Pérez, R., Latorre-Pellicer, A., Colás, C., Balsa, E., Perales-Clemente, E., Quirós, P.M., Calvo, E., Rodríguez-Hernández, M.A., et al. (2013). Supercomplex assembly determines electron flux in the mitochondrial electron transport chain. Science *340*, 1567–1570. https://doi.org/10.1126/science.1230381.

Lenaz, G., and Genova, M.L. (2007). Kinetics of integrated electron transfer in the mitochondrial respiratory chain: random collisions vs. solid state electron channeling. Am. J. Physiol. Cell Physiol. *292*, C1221–C1239. https://doi.org/10.1152/ajpcell.00263.2006.

Lenaz, G., and Genova, M.L. (2009). Mobility and function of coenzyme Q (ubiquinone) in the mitochondrial respiratory chain. Biochim. Biophys. Acta *1787*, 563–573. https://doi.org/10.1016/j.bbabio.2009.02.019.

Letts, J.A., and Sazanov, L.A. (2017). Clarifying the supercomplex: the higher-order organization of the mitochondrial electron transport chain. Nat. Struct. Mol. Biol. *24*, 800–808. https://doi.org/10.1038/nsmb.3460.

Letts, J.A., Fiedorczuk, K., and Sazanov, L.A. (2016). The architecture of respiratory supercomplexes. Nature *537*, 644–648. https://doi.org/10.1038/nature19774.

Letts, J.A., Fiedorczuk, K., Degliesposti, G., Skehel, M., and Sazanov, L.A. (2019). Structures of respiratory supercomplex I+III_2 reveal functional and conformational crosstalk. Mol. Cell *75*, 1131–1146.e6. https://doi.org/10.1016/j.molcel.2019.07.022.

Livak, K.J., and Schmittgen, T.D. (2001). Analysis of relative gene expression data using real-time quantitative PCR and the $2^{-\Delta\Delta C}{}_T$ method. Methods *25*, 402–408. https://doi.org/10.1006/meth.2001.1262.

Lobo-Jarne, T., and Ugalde, C. (2018). Respiratory chain supercomplexes: structures, function and biogenesis. Semin. Cell Dev. Biol. *76*, 179–190. https://doi.org/10.1016/j.semcdb.2017.07.021.

Lobo-Jarne, T., Nývltová, E., Pérez-Pérez, R., Timón-Gómez, A., Molinié, T., Choi, A., Mourier, A., Fontanesi, F., Ugalde, C., and Barrientos, A. (2018). Human COX7A2L regulates complex III biogenesis and promotes supercomplex organization remodeling without affecting mitochondrial bioenergetics. Cell Rep. *25*, 1786–1799.e4. https://doi.org/10.1016/j.celrep.2018.10.058.

Lobo-Jarne, T., Pérez-Pérez, R., Fontanesi, F., Timón-Gómez, A., Wittig, I., Peñas, A., Serrano-Lorenzo, P., García-Consuegra, I., Arenas, J., Martín, M.A., et al. (2020). Multiple pathways coordinate assembly of human mitochondrial complex IV and stabilization of respiratory supercomplexes. EMBO J. *39*, e103912. https://doi.org/10.15252/embj.2019103912.

Lopez-Fabuel, I., Le Douce, J., Logan, A., James, A.M., Bonvento, G., Murphy, M.P., Almeida, A., and Bolaños, J.P. (2016). Complex I assembly into supercomplexes determines differential mitochondrial ROS production in neurons and astrocytes. Proc. Natl. Acad. Sci. USA *113*, 13063–13068. https://doi.org/10.1073/pnas.1613701113.

Milenkovic, D., Blaza, J.N., Larsson, N.G., and Hirst, J. (2017). The enigma of the respiratory chain supercomplex. Cell Metab. *25*, 765–776. https://doi.org/10.1016/j.cmet.2017.03.009.

Molinié, T., Cougouilles, E., David, C., Cahoreau, E., Portais, J.C., and Mourier, A. (2022). MDH2 produced OAA is a metabolic switch rewiring the fuelling of respiratory chain and TCA cycle. Biochim. Biophys. Acta Bioenerg. *1863*, 148532. https://doi.org/10.1016/j.bbabio.2022.148532.

Moreno-Lastres, D., Fontanesi, F., García-Consuegra, I., Martín, M.A., Arenas, J., Barrientos, A., and Ugalde, C. (2012). Mitochondrial complex I plays an essential role in human respirasome assembly. Cell Metab. *15*, 324–335. https://doi.org/10.1016/j.cmet.2012.01.015.

Mourier, A., Matic, S., Ruzzenente, B., Larsson, N.G., and Milenkovic, D. (2014). The respiratory chain supercomplex organization is independent of COX7a2l isoforms. Cell Metab. *20*, 1069–1075. https://doi.org/10.1016/j.cmet.2014.11.005.

Nijtmans, L.G.J., Henderson, N.S., and Holt, I.J. (2002). Blue Native electrophoresis to study mitochondrial and other protein complexes. Methods *26*, 327–334.

Ogunjimi, E.O., Pokalsky, C.N., Shroyer, L.A., and Prochaska, L.J. (2000). Evidence for a conformational change in subunit III of bovine heart mitochondrial cytochrome c oxidase. J. Bioenerg. Biomembr. *32*, 617–626. https://doi.org/10.1023/a:1005678729157.

Páleníková, P., Harbour, M.E., Ding, S., Fearnley, I.M., Van Haute, L., Rorbach, J., Scavetta, R., Minczuk, M., and Rebelo-Guiomar, P. (2021a). Quantitative density gradient analysis by mass spectrometry (qDGMS) and complexome profiling analysis (ComPrAn) R package for the study of macromolecular complexes. Biochim. Biophys. Acta Bioenerg. *1862*, 148399. https://doi.org/10.1016/j.bbabio.2021.148399.

Páleníková, P., Harbour, M.E., Prodi, F., Minczuk, M., Zeviani, M., Ghelli, A., and Fernández-Vizarra, E. (2021b). Duplexing complexome profiling with SILAC to study human respiratory chain assembly defects. Biochim. Biophys. Acta Bioenerg. *1862*, 148395. https://doi.org/10.1016/j.bbabio.2021.148395.

Pérez-Pérez, R., Lobo-Jarne, T., Milenkovic, D., Mourier, A., Bratic, A., García-Bartolomé, A., Fernández-Vizarra, E., Cadenas, S., Delmiro, A., García-Consuegra, I., et al. (2016). COX7A2L is a mitochondrial complex III binding protein that stabilizes the III_2+IV supercomplex without affecting respirasome formation. Cell Rep. *16*, 2387–2398. https://doi.org/10.1016/j.celrep.2016.07.081.

Pesta, D., and Gnaiger, E. (2012). High-resolution respirometry: OXPHOS protocols for human cells and permeabilized fibers from small biopsies of human muscle. Methods Mol. Biol. *810*, 25–58. https://doi.org/10.1007/978-1-61779-382-0_3.

Protasoni, M., Pérez-Pérez, R., Lobo-Jarne, T., Harbour, M.E., Ding, S., Peñas, A., Diaz, F., Moraes, C.T., Fearnley, I.M., Zeviani, M., et al. (2020). Respiratory supercomplexes act as a platform for complex III-mediated maturation of human mitochondrial complexes I and IV. EMBO J. *39*, e102817. https://doi.org/10.15252/embj.2019102817.

Ran, F.A., Hsu, P.D., Wright, J., Agarwala, V., Scott, D.A., and Zhang, F. (2013). Genome engineering using the CRISPR-Cas9 system. Nat. Protoc. *8*, 2281–2308. https://doi.org/10.1038/nprot.2013.143.

Robinson, B.H., Petrova-Benedict, R., Buncic, J.R., and Wallace, D.C. (1992). Nonviability of cells with oxidative defects in galactose medium: a screening test for affected patient fibroblasts. Biochem. Med. Metab. Biol. *48*, 122–126. https://doi.org/10.1016/0885-4505(92)90056-5.

Schägger, H., and Pfeiffer, K. (2000). Supercomplexes in the respiratory chains of yeast and mammalian mitochondria. EMBO J. *19*, 1777–1783. https://doi.org/10.1093/emboj/19.8.1777.

Schell, J.C., Olson, K.A., Jiang, L., Hawkins, A.J., Van Vranken, J.G., Xie, J., Egnatchik, R.A., Earl, E.G., DeBerardinis, R.J., and Rutter, J. (2014). A role for the mitochondrial pyruvate carrier as a repressor of the Warburg effect and colon cancer cell growth. Mol. Cell *56*, 400–413. https://doi.org/10.1016/j.molcel.2014.09.026.

Schell, J.C., Wisidagama, D.R., Bensard, C., Zhao, H., Wei, P., Tanner, J., Flores, A., Mohlman, J., Sorensen, L.K., Earl, C.S., et al. (2017). Control of

intestinal stem cell function and proliferation by mitochondrial pyruvate metabolism. Nat. Cell Biol. *19*, 1027–1036. https://doi.org/10.1038/ncb3593.

Schneider, C.A., Rasband, W.S., and Eliceiri, K.W. (2012). NIH Image to ImageJ: 25 years of image analysis. Nat. Methods *9*, 671–675.

Shiba, S., Ikeda, K., Horie-Inoue, K., Nakayama, A., Tanaka, T., and Inoue, S. (2017). Deficiency of COX7RP, a mitochondrial supercomplex assembly promoting factor, lowers blood glucose level in mice. Sci. Rep. *7*, 7606. https://doi.org/10.1038/s41598-017-08081-z.

Sinkler, C.A., Kalpage, H., Shay, J., Lee, I., Malek, M.H., Grossman, L.I., and Hüttemann, M. (2017). Tissue- and condition-specific isoforms of mammalian cytochrome c oxidase subunits: From function to human disease. Oxid. Med. Cell. Longev. *2017*, 1534056. https://doi.org/10.1155/2017/1534056.

Smith, A.C., and Robinson, A.J. (2019). MitoMiner v4.0: an updated database of mitochondrial localization evidence, phenotypes and diseases. Nucleic Acids Res. *47*, D1225–D1228. https://doi.org/10.1093/nar/gky1072.

Sorge, S., Theelke, J., Yildirim, K., Hertenstein, H., McMullen, E., Müller, S., Altbürger, C., Schirmeier, S., and Lohmann, I. (2020). ATF4-induced Warburg metabolism drives over-proliferation in *Drosophila*. Cell Rep. *31*, 107659. https://doi.org/10.1016/j.celrep.2020.107659.

Sousa, J.S., Mills, D.J., Vonck, J., and Kühlbrandt, W. (2016). Functional asymmetry and electron flow in the bovine respirasome. eLife *5*, e21290. https://doi.org/10.7554/eLife.21290.

Stacpoole, P.W. (2017). Therapeutic targeting of the pyruvate dehydrogenase complex/pyruvate dehydrogenase kinase (PDC/PDK) axis in cancer. J. Natl. Cancer Inst. *109*, djx071. https://doi.org/10.1093/jnci/djx071.

Stroud, D.A., Surgenor, E.E., Formosa, L.E., Reljic, B., Frazier, A.E., Dibley, M.G., Osellame, L.D., Stait, T., Beilharz, T.H., Thorburn, D.R., et al. (2016). Accessory subunits are integral for assembly and function of human mitochondrial complex I. Nature *538*, 123–126. https://doi.org/10.1038/nature19754.

Stuchebrukhov, A., Schäfer, J., Berg, J., and Brzezinski, P. (2020). Kinetic advantage of forming respiratory supercomplexes. Biochim. Biophys. Acta Bioenerg. *1861*, 148193. https://doi.org/10.1016/j.bbabio.2020.148193.

Szibor, M., Gainutdinov, T., Fernandez-Vizarra, E., Dufour, E., Gizatullina, Z., Debska-Vielhaber, G., Heidler, J., Wittig, I., Viscomi, C., Gellerich, F., and Moore, A. (2020). Bioenergetic consequences from xenotopic expression of a tunicate AOX in mouse mitochondria: switch from RET and ROS to FET. Biochim. Biophys. Acta Bioenerg. *1861*, 148137. https://doi.org/10.1016/j.bbabio.2019.148137.

Tataranni, T., Agriesti, F., Pacelli, C., Ruggieri, V., Laurenzana, I., Mazzoccoli, C., Sala, G.D., Panebianco, C., Pazienza, V., Capitanio, N., and Piccoli, C. (2019). Dichloroacetate affects mitochondrial function and stemness-associated properties in pancreatic cancer cell lines. Cells *8*, 478. https://doi.org/10.3390/cells8050478.

Timón-Gómez, A., Garlich, J., Stuart, R.A., Ugalde, C., and Barrientos, A. (2020). Distinct roles of mitochondrial HIGD1A and HIGD2A in respiratory complex and supercomplex biogenesis. Cell Rep. *31*, 107607. https://doi.org/10.1016/j.celrep.2020.107607.

Trouillard, M., Meunier, B., and Rappaport, F. (2011). Questioning the functional relevance of mitochondrial supercomplexes by time-resolved analysis of the respiratory chain. Proc. Natl. Acad. Sci. USA *108*, E1027–E1034. https://doi.org/10.1073/pnas.1109510108.

Tyanova, S., Temu, T., Sinitcyn, P., Carlson, A., Hein, M.Y., Geiger, T., Mann, M., and Cox, J. (2016). The Perseus computational platform for comprehensive analysis of (prote)omics data. Nat. Methods *13*, 731–740. https://doi.org/10.1038/nmeth.3901.

van Strien, J., Haupt, A., Schulte, U., Braun, H.P., Cabrera-Orefice, A., Choudhary, J.S., Evers, F., Fernández-Vizarra, E., Guerrero-Castillo, S., Kooij, T.W.A., et al. (2021). CEDAR, an online resource for the reporting and exploration of complexome profiling data. Biochim. Biophys. Acta Bioenerg. *1862*, 148411. https://doi.org/10.1016/j.bbabio.2021.148411.

Vercellino, I., and Sazanov, L.A. (2021). Structure and assembly of the mammalian mitochondrial supercomplex $CIII_2CIV$. Nature *598*, 364–367. https://doi.org/10.1038/s41586-021-03927-z.

Vercellino, I., and Sazanov, L.A. (2022). The assembly, regulation and function of the mitochondrial respiratory chain. Nat. Rev. Mol. Cell Biol. *23*, 141–161. https://doi.org/10.1038/s41580-021-00415-0.

Vidoni, S., Harbour, M.E., Guerrero-Castillo, S., Signes, A., Ding, S., Fearnley, I.M., Taylor, R.W., Tiranti, V., Arnold, S., Fernández-Vizarra, E., and Zeviani, M. (2017). MR-1S interacts with PET100 and PET117 in module-based assembly of human cytochrome c oxidase. Cell Rep. *18*, 1727–1738. https://doi.org/10.1016/j.celrep.2017.01.044.

Villani, G., and Attardi, G. (2000). In vivo control of respiration by cytochrome c oxidase in human cells. Free Radic. Biol. Med. *29*, 202–210. https://doi.org/10.1016/s0891-5849(00)00303-8.

Villani, G., Greco, M., Papa, S., and Attardi, G. (1998). Low reserve of cytochrome c oxidase capacity in vivo in the respiratory chain of a variety of human cell types. J. Biol. Chem. *273*, 31829–31836. https://doi.org/10.1074/jbc.273.48.31829.

Wu, M., Gu, J., Guo, R., Huang, Y., and Yang, M. (2016). Structure of mammalian respiratory supercomplex $I_1III2IV1$. Cell *167*, 1598–1609.e10. https://doi.org/10.1016/j.cell.2016.11.012.

Zhang, K., Wang, G., Zhang, X., Hüttemann, P.P., Qiu, Y., Liu, J., Mitchell, A., Lee, I., Zhang, C., Lee, J.S., et al. (2016). COX7AR is a stress-inducible mitochondrial COX subunit that promotes breast cancer malignancy. Sci. Rep. *6*, 31742. https://doi.org/10.1038/srep31742.

Zong, S., Wu, M., Gu, J., Liu, T., Guo, R., and Yang, M. (2018). Structure of the intact 14-subunit human cytochrome c oxidase. Cell Res. *28*, 1026–1034. https://doi.org/10.1038/s41422-018-0071-1.

Please cite this article in press as: Fernández-Vizarra et al., Two independent respiratory chains adapt OXPHOS performance to glycolytic switch, Cell Metabolism (2022), https://doi.org/10.1016/j.cmet.2022.09.005

STAR★METHODS

KEY RESOURCES TABLE

REAGENT or RESOURCE	SOURCE	IDENTIFIER
Antibodies		
Mouse monoclonal anti-NDUFA9	Abcam	Cat#ab14713; RRID: AB_301431
Rabbit polyclonal anti-NDUFV1	Proteintech	Cat#11238-1-AP; RRID: AB_2149040
Mouse monoclonal anti-SDHA	Abcam	Cat#ab14715; RRID: AB_301433
Mouse monoclonal anti-UQCRC2 (CORE2)	Abcam	Cat#ab14745; RRID: AB_2213640
Mouse monoclonal anti-UQCRC1 (CORE1)	Sigma	Cat# SAB1406570; RRID: AB_10741550
Rabbit polyclonal anti-COX7A2L	Proteintech	Cat#11416-1-AP; RRID: AB_2245402
Mouse monoclonal anti-MTCO1	Abcam	Cat#ab14705; RRID: AB_2084810
HRP-conjugated mouse monoclonal anti-COX4	Abcam	Cat#ab62164; RRID: AB_2085277
Mouse monoclonal anti-COX5A	Abcam	Cat# ab110262; RRID: AB_10861723
Mouse monoclonal anti-COX5B	Santa Cruz	Cat#sc-374417; RRID: AB_10988066
Rabbit polyclonal anti-COX6B1	Proteintech	Cat#11425-1-AP; RRID: AB_2085449
PhosphoDetect Anti-PDH-E1α (pSer^{232}) Rabbit pAb	Sigma-Aldrich	Cat#AP1063; RRID: AB_10616070
Mouse monoclonal anti-DDK (FLAG)	Sigma-Aldrich	Cat#TA50011; RRID: AB_2622345
Mouse monoclonal anti-β-actin	Sigma-Aldrich	Cat#A1978; RRID: AB_476692
HRP-conjugated goat anti-mouse IgG	Invitrogen	Cat#G21040; RRID: AB_2536527
HRP-conjugated goat anti-rabbit IgG	Invitrogen	Cat#G21234; RRID: AB_2536530
Biological samples		
Brain post-mortem tissue; Sex distribution: 2 males, 1 female; Age range: 86-87 yrs	Haukeland University Hospital, Bergen, Norway.	N/A
Skeletal muscle biopsy; Sex: Unknown	UCL Queen Square Institute of Neurology, London, UK.	N/A
Chemicals, peptides, and recombinant proteins		
DMEM	Gibco	Cat#31966
DMEM for SILAC	Gibco	Cat#88364
L-Lysine-$^{13}C_6$,$^{15}N_2$ hydrochloride	Sigma-Aldrich	Cat#608041
L-Arginine-$^{13}C_6$,$^{15}N_4$ hydrochloride	Sigma-Aldrich	Cat#608033
L-Lysine monohydrochloride	Sigma-Aldrich	Cat#L8662
L-Arginine	Sigma-Aldrich	Cat#A8094
L-Proline	Sigma-Aldrich	Cat#P5607
Uridine	Sigma-Aldrich	Cat#U3003
Fetal Bovine Serum (FBS)	Gibco	Cat#10270
Dialyzed FBS	Gibco	Cat#26400
Hygromycin B	Invitrogen	Cat#10687010
Doxycycline	Sigma-Aldrich	Cat#D9891
Cycloheximide	Sigma-Aldrich	Cat#C1988
Digitonin, High Purity	Calbiochem	Cat#300410
n-Dodecyl-beta-maltoside (DDM)	Sigma-Aldrich	Cat#D4641
Sodium dichloroacetate (DCA)	Sigma-Aldrich	Cat#347795
TRizol Reagent	Invitrogen	Cat#15596026
Protease Inhibitor Cocktail	Roche	Cat#04693124001
XF DMEM Medium	Agilent	Cat#103575-100
Poly-D-lysine	Sigma-Aldrich	Cat#A-003-M

(*Continued on next page*)

Please cite this article in press as: Fernández-Vizarra et al., Two independent respiratory chains adapt OXPHOS performance to glycolytic switch, Cell Metabolism (2022), https://doi.org/10.1016/j.cmet.2022.09.005

Continued

REAGENT or RESOURCE	SOURCE	IDENTIFIER
Oligomycin	Sigma-Aldrich	Cat#O4876
CCCP	Sigma-Aldrich	Cat#C2759
Pyruvate	Sigma-Aldrich	Cat#P2256
Glutamate	Sigma-Aldrich	Cat#G1626
Malate	Sigma-Aldrich	Cat#M9138
Rotenone	Sigma-Aldrich	Cat#R8875
Succinate	Sigma-Aldrich	Cat#S2378
Glycerol-3-phosphate	Sigma-Aldrich	Cat#G7886
Antimycin A	Sigma-Aldrich	Cat#A8674
TMPD	Sigma-Aldrich	Cat#T3134
Ascorbic Acid	Sigma-Aldrich	Cat#A5960
KCN	Sigma-Aldrich	Cat#60178
NADH	Roche	Cat#10107735001
Nitrotetrazolium Blue chloride	Sigma-Aldrich	Cat#N6876
3,3′-Diaminobenzidine tetrahydrochloride hydrate	Sigma-Aldrich	Cat#D5637
Cytochrome c from equine heart	Sigma-Aldrich	Cat#C7552
Catalase from bovine liver	Sigma-Aldrich	Cat#C100
Ferritin from equine spleen	Sigma-Aldrich	Cat#F4503
Precision Plus Protein Dual Color Standards	BioRad	Cat#1610374
Critical commercial assays		
SuperScript IV First-Strand Synthesis System	Invitrogen	Cat#18091050
Fast SYBR Green Master Mix	Applied Biosystems	Cat#4385612
Pierce BCA protein assay kit	Thermo Scientific	Cat#23225
MitoPlate S-1	Biolog	Cat#14105
CyQUANT assay kit	Invitrogen	Cat#C7026
ECL Prime Western Blotting Detection Reagent	Cytiva-Amersham	Cat#RPN2236
Deposited data		
SILAC-Complexome Profiling WT vs SCAFIKO#1	CEDAR (van Strien et al., 2021) https://www3.cmbi.umcn.nl/cedar/browse/	CRX28
SILAC-Complexome Profiling WT vs COX7A2KO#7	CEDAR	CRX29
SILAC-Complexome Profiling WT vs DKO#8	CEDAR	CRX30
SILAC-Complexome Profiling WT vs DKO#9	CEDAR	CRX31
Experimental models: Cell lines		
Human HEK293T	ATCC	Cat#CRL-3216
Human HEK293T-SCAFI^{KO} (Clone #1 and #9)	Fernández-Vizarra et al., 2021	N/A
Human HEK293T-COX7A2^{KO} (Clone #7 and #10)	This work	N/A
Human HEK293T-D^{KO} (Double KO for SCAFI and COX7A2; Clone #8 and #9)	This work	N/A
Human Fibroblasts *PDHA1* c.[910C>T];[=]; Protein change: p.Arg304Ter; Basal PDH activity: 79.4% of average control values; Sex: Female	Cell line and DNA Bank of Disorders and Mitochondrial Diseases (GMD-MDbank), Milan, Italy.	PD07

(*Continued on next page*)

Please cite this article in press as: Fernández-Vizarra et al., Two independent respiratory chains adapt OXPHOS performance to glycolytic switch, Cell Metabolism (2022), https://doi.org/10.1016/j.cmet.2022.09.005

Continued

REAGENT or RESOURCE	SOURCE	IDENTIFIER
Human Fibroblasts *PDHA1* c.[628A>G];[0]; Protein change: p.Met210Val; Basal PDH activity: 19% of average control values; Sex: Male	GMD-MDbank	PD43
Human Fibroblasts *PDHA1* c.[499G>A];[0]; Protein change: p.Val167Met; Basal PDH activity: 45.2% of average control values; Sex: Female	GMD-MDbank	PD59
Control Human Fibroblasts; Sex: Unknown	Hospital 12 de Octubre (H12O), Madrid, Spain	CP1
Control Human Fibroblasts; Sex: Male	H12O	CN1
Control Human Fibroblasts; Sex: Unknown	H12O	22211
Oligonucleotides		
SCAFI-Forward: 5'-TTCACGCAGAAGTTGGCAGG-3'	This paper	N/A
SCAFI-Reverse: 5'-GAGGTCAGTTTAGTTGGTGTGG-3'	This paper	N/A
HPRT1-Forward: 5'-CCTGGCGTCGTGATTAGTGA-3'	This paper	N/A
HPRT1-Reverse: 5'-CGAGCAAGACGTTCAGTCCT-3'	This paper	N/A
Recombinant DNA		
pSp-CAS9(BB)-2A-GFP (PX458)	Ran et al., 2013	Addgene# 48138
COX7A2L- Myc-DDK	Origene	Cat#RC202697
COX7A1- Myc-DDK	Origene	Cat#RC201154
COX7A2- Myc-DDK	Origene	Cat#RC215973
pCMV6-A-Entry-Hygro	Origene	Cat# PS100024
COX7A2L-Myc-DDK in pCMV6-A-Entry-Hygro	Lobo-Jarne et al., 2018	N/A
COX7A1- Myc-DDK in pCMV6-A-Entry-Hygro	This paper	N/A
COX7A2- Myc-DDK in pCMV6-A-Entry-Hygro	This paper	N/A
Software and algorithms		
GraphPad Prism v.8-v.9	GraphPad Software	https://www.graphpad.com/scientific-software/prism/
Seahorse Wave Software v.2.6	Agilent	https://www.agilent.com/en/product/cell-analysis/real-time-cell-metabolic-analysis/xf-software/
ImageJ	Schneider et al., 2012	http://imagej.net
MaxQuant v1.6.10.43	Cox and Mann, 2008	https://www.maxquant.org/
Perseus v1.6.10.43	Tyanova et al., 2016	https://www.maxquant.org/perseus/
Proteome Discoverer	Thermo Scientific	Cat# OPTON-30945
SILAC-Complexome Profiling Analysis Scripts	Páleníková et al., 2021a; 2021b	https://github.com/Scavetta/ComPrAn
Other		
Amersham Protran NC Nitrocellulose Membranes	GE Hrcealthcare Life Sciences	Cat#15259794
Immobilon-P PVDF Membrane	Sigma-Aldrich	Cat#IPVH00010
NativePAGE 3–12% Bis-Tris Gels	Invitrogen	Cat#BN1001BOX
NuPAGE 12% Bis-Tris Gels	Invitrogen	Cat#NP0341PK2

Please cite this article in press as: Fernández-Vizarra et al., Two independent respiratory chains adapt OXPHOS performance to glycolytic switch, Cell Metabolism (2022), https://doi.org/10.1016/j.cmet.2022.09.005

CellPress

RESOURCE AVAILABILITY

Lead contact

Further information and requests for resources and reagents should be directed to and will be fulfilled by the Lead Contact, Dr. Cristina Ugalde (cugalde@h12o.es).

Materials availability

All the materials generated and used in this study will be available upon request.

Data and code availability

- Complexome profiling data from human cell lines have been deposited at the ComplexomE profiling DAta Resource (CEDAR) repository (van Strien et al., 2021) and are publicly available as of the date of publication. Accession numbers are listed in the key resources table. Proteomic data and complexome profiles from cells and human tissues have been deposited to the Mendeley archive (https://doi.org/10.17632/spsg756sx8.1). Uncropped western blots and original data for creating all graphs in the paper are provided in Data S1.
- No original code was generated in this study.
- Any additional information required to reanalyze the data reported in this paper is available from the lead contact upon request.

EXPERIMENTAL MODEL AND SUBJECT DETAILS

Human cell lines and primary fibroblasts

Parental HEK293T and the derived cell lines, as well as PDH-deficient and control primary fibroblasts (detailed in the key resources table), were cultured in high-glucose (4.5 g/l) DMEM containing sodium pyruvate and GlutaMAX, supplemented with 10% fetal bovine serum (FBS) and 50 μg/ml uridine. All cell lines were kept in a humidified incubator at 37°C and 5% CO_2.

Human tissues

Brain tissue was collected post-mortem (autopsy) from neurologically healthy individuals. A skeletal muscle biopsy was collected from a patient with a low suspicion of an underlying muscle disorder, and subsequent normal muscle histology and histochemical examination (including no COX-negative or ragged red fibers). Research involving human samples was performed in accordance with the Declaration of Helsinki, and approved by the Queen Square Research Ethics Committee, London, UK (09/H0716/76), and by the Regional Committee for Medical and Health Research Ethics, Western-Norway, Norway (REK, references 2017/2082 and 2010/1700). Consent for publication was provided by all participants.

METHOD DETAILS

Cell culture

Cells used in SILAC experiments were grown in DMEM for SILAC (Gibco-Thermo Fisher Scientific) plus 10% dialyzed serum (Gibco-Thermo Fisher Scientific) and 50 μg/ml uridine, supplemented either with unlabeled L-lysine monohydrochloride (K_0), L-arginine (R_0) and L-proline ('Light' conditions) or with L-lysine-$^{13}C_6$,$^{15}N_2$ hydrochloride (K_8), L-arginine-$^{13}C_6$,$^{15}N_4$ hydrochloride (R_{10}) and L-proline ('Heavy' conditions), all from Sigma-Aldrich.

Cells were transiently transfected with the pCMV6-Entry and pCMV6-COX7A-Myc-DDK vectors using Lipofectamine 2000 (ThermoFisher) according to the manufacturer's instructions, and collected after 48 hours for subsequent analyses. Cells transduced with expression vectors containing a hygromycin resistance cassette were grown in the presence of 50 μg/ml hygromycin (Invitrogen). To assess SCAFI stability, cells were treated with 200 μg/ml of the protein synthesis inhibitor cycloheximide (CHX). To follow the assembly kinetics of MRC complexes and SCs, cells were treated with doxycycline, a reversible inhibitor of mitochondrial translation, as previously reported (Moreno-Lastres et al., 2012). For PDH activation, cells were treated with 30 mM of the PDK inhibitor dichloroacetate (DCA) for up to 96-168 hrs.

Gene editing and Screening

Gene editing was performed using the pSp-CAS9(BB)-2A-GFP (PX458) CRISPR/Cas9 construct (gift from F. Zhang; Addgene plasmid 48138) (Ran et al., 2013). CRISPR/Cas9 guide RNAs were designed using CHOPCHOP v2 (Labun et al., 2016). Target sequences, gene disruption strategies and generated indels are described in Figure S1A and Fernandez-Vizarra et al. (2021).

Real time quantitative PCR

Total RNA was extracted with TRIzol reagent (Invitrogen). Complementary DNA (cDNA) was generated from 2 μg of RNA samples by using SuperScript IV First-Strand Synthesis System (Promega) as per the manufacturer's instructions. RT-qPCR was performed in triplicate per sample with the Fast SYBR Green Master (Roche) using 500 nM of specific primers for *SCAFI* mRNA (Forward: 5'- TTCACGCAGAAGTTGGCAGG-3' and Reverse: 5'- GAGGTCAGTTTAGTTGGTGTGG-3') on a Light cycler 96 real-time PCR

system (Roche Life Science). The 2-ΔΔCt method (Livak and Schmittgen, 2001) was used to determine *SCAFI* mRNA levels normalised by the mRNA levels of the housekeeping gene *HPRT1* (Hypoxanthine phosphoribosyltransferase 1; Forward: 5'-CCT GGC GTC GTG ATT AGT GA-3' and Reverse: 5'-CGA GCA AGA CGT TCA GTC CT-3').

Cell growth

Growth curves were assessed by cell counting using a Neubauer chamber. Cells growing in 24-wells plates were harvested and counted every 24 h in triplicate for periods up to 72-168 h.

Respirometry

Mitochondrial oxygen consumption rates were measured in live cells using a Seahorse Bioscience XFe-96 Analyzer (Agilent). Briefly, 25,000 cells were plated per well in culture plates treated with 50 μg/mL poly-D-lysine. For each assay cycle, there were 4 measurements of 2 minutes mixing, 2 minutes wait, and 5 minutes measure. The following inhibitor concentrations were used: 2 μM oligomycin, 0.5 μM carbonyl cyanide m-chlorophenylhydrazone (CCCP), 0.5 μM rotenone and 0.3 μM antimycin A. Data were normalised using the CyQUANT assay kit (Invitrogen) and analyzed using Wave (version 2.6.0, Agilent) and Prism (version 8.0.2, GraphPad) software packages.

For substrate driven oxygen consumption and for the evaluation of KCN sensitivity, measurements were performed in digitonin-permeabilized cells (Doerrier et al., 2018; Hofhaus et al., 1996) or intact cells, respectively, using an Oroboros High-Resolution Respirometer (Pesta and Gnaiger, 2012). Measurements were performed with a starting amount of approximately $2x10^6$ (intact) or 5×10^6 (permeabilized) cells. The oxygen consumption rates were normalized by cell number. In permeabilized cells, cells were counted before and after the digitonin treatment and the number of permeabilized cells present in the respiration chamber was used for the normalization.

Protein separation by SDS-PAGE and Immunoblotting

Protein extracts from cultured cells or mitochondrial fractions were homogenized in an extraction buffer containing 20 Mm HEPES NaOH pH 7,4, 150 mM NaCl, 10% glycerol and 1% Triton X-100, supplemented with a Protease Inhibitor Cocktail (Roche). Protein concentration was measured with the BCA protein assay kit (ThermoFisher). Protein extracts (30-50 μg) were separated on 10% SDS-PAGE gels and transferred to PROTAN (Schleicher & Schuell) nitrocellulose membranes by conventional procedures.

Blue Native Electrophoresis and In-Gel Activity Assays

Mitochondrial pellets were isolated from P150 cell culture flasks or 15-cm dishes (ThermoFisher) as described before (Lobo-Jarne et al., 2020). Unless otherwise indicated, samples were solubilized using digitonin and n-Dodecyl β-D-maltoside at a detergent-to-protein ratio of 4:1 and 2:1, respectively. Pre-cast NativePAGE 3-12% Bis-Tris gels (Invitrogen) were loaded with 60-80 μg of mitochondrial protein and processed for blue native electrophoresis (BN-PAGE) as previously described (Moreno-Lastres et al., 2012). After electrophoresis, proteins were transferred to nitrocellulose membranes at 40 V overnight and probed with antibodies. Duplicate gels were used for CI and CIV IGA assays.

Antibody detection

Western blots were performed using primary antibodies raised against either respiratory chain complex subunits, the FLAG tag or β-actin. The immunoreactive bands were detected with horse radish peroxidase (HRP) conjugated secondary antibodies and ECL Prime Western Blotting Detection Reagent in a ChemiDoc MP Imager (BioRad).

Acquisition and analysis of mass spectrometry data from HEK293T cells

LC MS/MS was carried out on a Q Exactive Plus Orbitrap mass spectrometer (Thermo Scientific) with a nanoESI interface in conjunction with an Ultimate 3000 RSLC nanoHPLC (Dionex Ultimate 3000). The LC system was equipped with an Acclaim Pepmap nanotrap column (Dionex-C18, 100 Å, 75 μm x 2 cm) and an Acclaim Pepmap RSLC analytical column (Dionex-C18, 100 Å, 75 μm x 50 cm). The tryptic peptides were injected to the enrichment column at an isocratic flow of 3 μL/min of 2% (v/v) ACN containing 0.1% (v/v) formic acid for 5 min applied before the enrichment column was switched in-line with the analytical column. The eluents were 5% DMSO in 0.1% (v/v) formic acid (solvent A) and 5% DMSO in 100% v/v ACN and 0.1% (v/v) formic acid (solvent B). The flow gradient was: (i) 0-6 min at 3% B, (ii) 6-95 min at 3-22% B, (iii) 95-105 min at 22-40% B, (iv) 105-110 min at 40-80% B (v) 110-115 min at 80-80% B, (vi) 115-117 min at 80-3% B, and equilibrated at 3% B for 10 min before the next sample injection. The mass spectrometer was operated in the data-dependent mode. Full MS1 spectra were acquired in positive mode, 70 000 resolution, AGC target of 3e6 and maximum IT time of 50ms. A loop count of 15 on the most intense targeted peptide were isolated for MS/MS. The isolation window was set at 1.2m/z and precursors fragmented using stepped normalized collision energy of 28, 30 and 32. MS2 Resolution was at 17 500, AGC target at 5e4 and maximum IT time of 50ms. Dynamic exclusion was set to be 30 sec.

Raw files were processed using the MaxQuant platform (v1.6.10.43) (Cox and Mann, 2008) and searched against UniProt human database (November 2019) using the settings previously reported (Stroud et al., 2016). Briefly, "re-quantify", "Match Between Runs" were enabled with default settings and "Label min. ratio count" set to "1". The proteinGroups.txt output from the search was processed in Perseus (v1.6.10.43) (Tyanova et al., 2016). Briefly, entries "Only identified by site", "Reverse" and "Potential contaminant" were removed from the data sets. Inverted ratios were first transformed "1/x", then Log_2-transformed and grouped ($SCAFI^{KO}$,

Please cite this article in press as: Fernández-Vizarra et al., Two independent respiratory chains adapt OXPHOS performance to glycolytic switch, Cell Metabolism (2022), https://doi.org/10.1016/j.cmet.2022.09.005

COX7A2^{KO}, D^{KO}) according to each experiment and filtered to have 2 out of 3 valid values in each group. The entire dataset was normalized using the ''Subtract row cluster'' function with ''Known mitochondrial'' entries from the IMPI (2017) database as reference (Smith and Robinson, 2019) and positive entries to Mitocarta2.0 (Calvo et al., 2016) database were annotated by gene name matching. One-sample *T-test*s were performed within groups using *P*-value for truncation (threshold *P*-value = 0.05). Rows not matched to the Mitocarta 2.0 database were removed prior to plotting the data as a volcano plot.

Complexome Profiling

Unlabeled enriched mitochondrial fractions from human tissues (Nijtmans et al., 2002) or mitochondria isolated from 1:1 mixtures of differentially SILAC labelled HEK293T WT and KO cells were used to analyze the samples and generate the complexome profiles as previously described (Páleníková et al., 2021b). The equal quantities of mixing of the Heavy and Light labels were checked by quantifying the relative amounts of the citrate synthase (CS) and TOM20 proteins (Protasoni et al., 2020; Páleníková et al., 2021b). In case of an obvious deviation in sample mixing, the peptides intensities were normalized using CS abundance.

Measurement of pyruvate consumption rates

The ability to transfer electrons from pyruvate to the MRC was evaluated in permeabilized cells using the MitoPlate S-1 technology (Biolog), following the manufacturer's instructions.

QUANTIFICATION AND STATISTICAL ANALYSIS

Biochemical experiments were performed at least in triplicate and results were presented as mean ± standard deviation (SD) values. When possible, in the bar graphs, the full data distribution was shown by overlaying the dot plots of the individual data points. All datasets passed the normality Shapiro-Will test and when $n \geq 5$, also the Kolmogorov-Smirnov test. Therefore, parametric tests were used to assess statistical *p* values, which were obtained by application of Student's t-test and one- or two-way ANOVA with Tukey's Multiple Comparisons test using the GraphPad Prism v.8.4.3-v.9.3.1 softwares. The relative protein abundances from the complexome profiling experiments were calculated as the mean ± standard error (SEM) of the two reciprocal labelled duplicate experiments. The areas under the curve were calculated using GraphPad Prism v.8.4.3-9.3.1. by simultaneously considering the peptide intensity profiles from two experimental replicates with 64 gel slices each. The statistical parameters can be found in the figures and figure legends.